Ann Kristin Lagmannsveen

De-icing coatings based on solar illumination

Preparation and characterisation

Master's thesis in Chemical Engineering and Biotechnology
Supervisor: Hilde Lea Lein
July 2020

Master's thesis

NTNU
Norwegian University of Science and Technology
Faculty of Natural Sciences
Department of Materials Science and Engineering

NTNU
Norwegian University of
Science and Technology

Ann Kristin Lagmannsveen

De-icing coatings based on solar illumination

Preparation and characterisation

Master's thesis in Chemical Engineering and Biotechnology
Supervisor: Hilde Lea Lein
July 2020

Norwegian University of Science and Technology
Faculty of Natural Sciences
Department of Materials Science and Engineering

NTNU
Norwegian University of
Science and Technology

Preface

This thesis is the result of the work carried out as part of the course *TMT4900 Materials Chemistry and Engineering Technology, Master's Thesis* at the Norwegian University of Science and Technology(NTNU). It is submitted as the final examination in a Master of Science degree within the field of Chemical Engineering and Biotechnology.

The work has been supervised by Associate Professor Hilde Lea Lein at the Department of Materials Science and Engineering, NTNU. The project had support from SINTEF Industry, and was co-supervised by SINTEF Research Scientist Sidsel Meli Hanetho. The integrating sphere measurements and calculations were carried out by PhD Candidate Håvard Wilson, and the DSC measurements were run by PhD Candidate Mohammad Adnan Mostafa, both at the Department of Materials Science and Engineering. SINTEF Research Engineer Anne Støre performed the thermal diffusivity measurements. The Research Council of Norway is acknowledged for the support to the Norwegian Micro- and Nano-Fabrication Facility, NorFab.

Trondheim, July 22nd 2020

Ann Kristin Lagmannsveen

Acknowledgements

I would first like to thank both Hilde and Sidsel for their excellent guidance throughout this last year. I know you are both very busy women who do your best to balance time spent on work and family. Nonetheless, you always took the time to answer any questions I might have had, and for that I am grateful.

Secondly, I want to thank friends and family for their continued, unconditional support. It is safe to say that the last couple of weeks leading up to the thesis deadline would have been very bleak without it. I am especially grateful to Clara, for proof reading my thesis, and to Vilde, for standing by my side and cheering me on towards the end of this unusually long semester. Thank you!

Appreciation should also be expressed to the Functional Materials and Materials Chemistry (FACET) research group, for all their constructive input, and to my fellow classmates for valuable discussions and for keeping my spirits high throughout this master semester. Thanks to the engineering staff at the Department of Materials Science and Enginerring, for instrument training and technical support. Thanks, also, to the Department of Chemistry for lending out your walk-in freezer to me so i could run my icing experiments.

Finally, the Covid-19 situation of this spring made it impossible for me to get the necessary training for all the instruments I needed to use in my characterisation study. Thanks to excellent help from Adnan, Håvard and Anne, I was still able to run all the measurements as planned, and for this I am ever grateful.

Abstract

The objective of this work was to prepare and characterise a type of coating designed for de-icing of surfaces exposed to freezing climates, such as wind turbines and aeroplanes. The coating consists of three layers interacting with each other in order to utilise the energy from incident illumination for ice mitigation. Such a coating could potentially be a more environmentally friendly alternative to de-icing methods used today, which are typically either energy-consuming or chemically polluting.

The most crucial and interesting properties of the de-icing coating lie with the surface layer, which purpose is to absorb incoming radiation and convert it to thermal energy. For this project, prototype coatings with four different surface layers were prepared using the ceramic tape casting method. One of the coatings was prepared with silicon carbide (SiC) as the surface layer; the other three were prepared with copper/cupric oxide cermet composites of varying metal content. Coating preparation by tape casting was demonstrated to be a simple and fair method of preparing samples for this kind of study. However, the durability of the coatings was observed to be far too poor for application purposes. Alternative preparation methods should thus be looked into, in order to produce a coating with denser and stronger surface layers.

The surface properties of the prototype coatings were characterised by scanning electron microscopy (SEM) and stylus profilometry. The wetting behaviour was analysed by water contact angle (WCA) measurements, and the durability investigated by scratch testing. Differential scanning calorimetry (DSC) and laser-flash measurements were used to calculate the thermal conductivities of the four surface materials, and their optical absorption properties were measured by integrating sphere spectroscopy. Finally, a simple experimental setup was used to characterise the de-icing properties of the four prototype coatings.

The characterisation study revealed several interesting findings. The surface structures of the prepared prototype coatings were measured to be very rough, but decreasingly so with decreased particle size in the material. This roughness was observed to have a strong influence on the wetting behaviour of the surfaces, and in turn, is thought to also have affected surface ice adhesion. The four surface layer materials were measured to have weak thermal conductivities, likely due to the high binder content and porosity. Their optical absorbance values were measured to be relatively high, which is a promising result with regards to their photothermal function. Results from the de-icing characterisation indicated that each of the four coatings, to varying extents, inherited the desired photothermal properties, as their performance was enhanced by illumination.

Sammendrag

Dette prosjektet har hatt som mål å lage og karakterisere et overflatebelegg som utnytter energien i solstråler til avising av flyvinger, vindmøller og andre installasjoner som er utsatt for isakkumulering. Belegget består av tre lag med ulike egenskaper, som virker sammen for å fjerne is som har samlet seg på overflaten ved hjelp av energien fra innfallende lys. Motivasjonen er at denne løsningen kan være et mer miljøvennlig alternativ til dagens avisingsmetoder, som er energikrevende og naturforurensende.

De viktigste, og mest interessante, egenskapene til belegget ligger i overflatelaget, hvis hensikt er å absorbere innkommende stråling og omforme det til varmeenergi. I dette arbeidet har fire prototyper av et slikt belegg blitt laget ved keramisk båndstøping. Ett av beleggene ble laget med silisiumkarbid som overflatelag; de tre andre med ulike komposisjoner av en kobber/kobber(II)oksid-kompositt. Båndstøping viste seg å være en enkel og rimelig metode for preparering av beleggsprøver til denne typen studie, men den produserer ikke belegg som er motstandsdyktige nok til å kunne anvendes i praksis. Videre arbeid bør av den grunn se til alternative preparative metoder som kan gi økt tetthet og styrke i beleggets overflatelag.

Beleggenes overflateegenskaper ble karakterisert ved sveipeelektronmikroskopi (SEM) og stylusprofilometri. Fuktegenskapene ble karakterisert ved vannkontakt-vinkelmålinger, og motstandsevnen ved skrapetesting. Målinger fra differensiell skanningskalorimetri (DSC) og laserflash ble brukt til å beregne termisk ledningsevne i de fire overflatematerialene, og deres optiske absorpsjonsegenskaper ble målt ved hjelp av integrerende kule-spektroskopi. Videre ble et enkelt eksperimentelt oppsett brukt for å karakterisere avisingsegenskapene til de fire prototypebeleggene.

Karakteriseringen avdekket flere interessante funn. For det første ble overflaten til beleggene målt til å være veldig ru, og at denne ruheten sank med redusert partikkelstørrelse i materialet. Den ru overflaten ble også observert til å ha hatt sterk innvirkning på fukteegenskapene til belegget, som igjen antas å være svært viktig for hvordan is heftes til overflaten. De fire overflatematerialene ble målt til å ha lav varmeledningsevne, trolig på grunn av porøsitet og høyt innhold av bindemiddel. Absorpsjonsevnen til materialene ble målt til å være tilstrekkelig høy, med hensyn til funksjonen de er ment å tjene. Resultatene fra avisingskarakteriseringen avdekket at bestråling fremmet avisingsegenskapene til samtlige prototypebelegg, noe som antyder at overflatematerialene innehar de nødvendige fototermiske egenskapene for formålet.

List of abbreviations and symbols

α	Thermal diffusivity
Cermet	Composite consisting of ceramic and metal components
$\mathbf{C}_p$	Specific heat capacity
γ	Interfacial tension
DSC	Differential scanning calorimetry
λ	Thermal conductivity
PSD	Particle size distribution
PVB	Polyvinyl butyral
$\mathbf{R}_a$	Arithmetic surface roughness
RT	Room temperature
ρ	Density
SEM	Scanning electron microscopy
T	Temperature
θ	Contact angle
$\mathbf{W}_A$	Work of adhesion
WCA	Water contact angle

Contents

Preface i

Acknowledgements iii

Abstract v

Sammendrag vii

List of abbreviations and symbols ix

1 Introduction 1
- 1.1 Ice mitigation tactics . . . 1
- 1.2 The photothermal trap . . . 3
- 1.3 Aim of the work . . . 4

2 Theory 5
- 2.1 Introduction to surface icing . . . 5
  - 2.1.1 Ice adhesion . . . 6
- 2.2 Solid surface wetting . . . 7
- 2.3 Optical absorption and photothermal conversion . . . 10
- 2.4 Material selection for the photothermal trap coating . . . 11
- 2.5 Methods of de-icing characterisation . . . 13

3 Experimental 15
- 3.1 Chemicals . . . 16
- 3.2 Sample preparation . . . 16
- 3.3 Powder characterisation . . . 19
- 3.4 Coating characterisation . . . 20
- 3.5 De-icing characterisation . . . 22
- 3.6 Optical and thermal characterisation . . . 25

4 Results 27
- 4.1 Coating characterisation . . . 27
  - 4.1.1 Surface roughness . . . 30
  - 4.1.2 Surface wetting . . . 31
  - 4.1.3 Coating hardness . . . 32
- 4.2 De-icing characterisation . . . 34
  - 4.2.1 Comparison of the three Cu/CuO coatings . . . 34
  - 4.2.2 Comparison of 50/50 Cu/CuO and SiC coatings . . . 36
- 4.3 Thermal characterisation . . . 38
- 4.4 Optical characterisation . . . 39

4.5 Powder characterisation 40
4.6 Sample density 42

5 Discussion **43**
5.1 Coating characteristics 43
5.1.1 Surface roughness 44
5.1.2 Wetting characteristics 45
5.1.3 Durability 46
5.2 Thermal properties 47
5.3 Optical properties 47
5.4 De-icing characteristics 48

6 Conclusion **51**

7 Further work **53**

References **55**

A Profilometer data and roughness calculations **I**

B Thermal measurements and calculations **VII**

C Sample density - measurements and calculations **IX**

1 Introduction

Many industries operating in freezing climates are faced with the challenge of ice build-up on structure surfaces [1–3]. The most obvious and talked about problems are, perhaps, within transportation. In the United States, icy and slushy pavements were reported as the cause of, on average, more than 300,000 car crashes annually between 2007 and 2016 [4]. Icing on aeroplanes is a serious issue, as any change to the aircraft surface heavily impacts the aerodynamics, which in turn decreases flight performance and fuel efficiency [5, 6]. Similar problems also appear in the energy sector, where icing of power transmission lines has always been a huge source of trouble [7]. With the rapidly increased interest in renewable energy over recent years, energy companies have also found that the development of wind farms in colder climates is not ideal. Ice accumulation on the wind turbines' blades drastically decreases their efficiency, and ice blocks falling to the ground can have fatal consequences for workers on site [8]. Due to all the negative aspects associated with surface icing, an enormous amount of resources is put into researching how to best defeat it.

Today, common methods of preventing and removing ice accumulation include electrical systems based on surface heating or mechanic removal, which require large amounts of energy. Depending on design and weather conditions, the anti-icing systems that are used in wind turbines sometimes require as much as a quarter of the electrical energy that is produced by the turbine [1]. In the fields of transport and aviation, the approach of lowering the water freezing point by use of salts and glycols is more common. Extensive use of such chemicals have been shown to negatively affect the environment and increase the rate of corrosion damage [9]. The ideal solution to the icing problem would be one that works efficiently, is gentle to the environment, requires minimal energy input, is inexpensive in use and easy to implement.

1.1 Ice mitigation tactics

When it comes to dealing with surface icing, the tactics used are generally categorised into two groups. The term de-icing is used when describing strategies to remove existing ice accumulation, whereas anti-icing strategies are put in place to prevent ice from forming on the surface to begin with [7, Ch.6]. There are advantages and disadvantages to both approaches, and different icing situations call for different solutions. For a wind turbine, thermal de-icing systems require less energy than thermal anti-icing systems, but the efficiency of the turbine is significantly lowered in the periods where ice is formed on the blades and not yet removed [1].

Ice mitigation systems like heating or mechanic removal, where an energy input is required, are also sometimes categorised as active. Most research today is focused on the development of so-called *passive* de-icing and anti-icing solutions. These get the job done without needing any external energy input other than from natural forces such as wind, gravity, solar irradiation, etc. This is achieved either by careful material selection, by modification of the surface structure, or by application of a coating layer. Most often, the mechanism for these solutions is focused on decreasing the strength of adhesion between the ice and the surface [10]. The concept behind this is that if the adhesion is weak enough, the ice can slide off either under its own weight or from a small external action such as a wind gust. Since ice is built from the same molecules as liquid water, a lot of the research within the field of anti-icing coatings is centred around developing water repellent or, in other words, hydrophobic surfaces. However, a clear correlation between a surfaces affinity towards ice and towards water is yet to be found [11, 12].

Previous studies have also looked at the possibility of amphiphilic coatings for anti-icing, where the surface has both hydrophobic and hydrophilic components [10]. The exact anti-icing mechanism for these surfaces is yet to be concluded upon, but a feasible theory is that a film of water remains unfrozen at the ice-coating interface, making the surface slippery. The main challenge of these passive coating solutions is in regards to the durability of the surfaces. Thin coatings and surface microstructures wear down quickly in harsh environments, and the ice mitigation effect decreases with every icing/de-icing cycle [13].

Electrostatic interactions between the ice and surface have been shown to contribute greatly to the adhesion, and thus extensive research has been put into developing anti-icing coatings made from polydimethylsiloxane (PDMS) and other insulating polymers. However, studies have revealed that this theory does not hold up as well in practice, and that the real case of ice adhesion is rather complex [14, 15].

More recently, research has shifted into the development of de-icing surfaces that utilise solar or auxiliary illumination by converting it into heat energy [2, 16, 17]. If such a coating functions efficiently, and can be produced from cheap, durable and sustainable materials, it could revolutionise the research on de-icing tactics.

1.2 The photothermal trap

Dash and his team of researchers at MIT have developed a coating that utilises incoming sunlight for de-icing purposes [2]. The coating consists of three layers that interact in a way that absorbs incident radiation and traps the energy as heat, which in turn causes an increase in temperature along the coating surface. This can melt av thin layer of ice at the ice/coating interface, creating a slippery water film which drastically lowers the ice adhesion. Thus, accumulated ice can slide off under its own weight or from a small, external nudge. The temperature rise also has an anti-icing effect because it slows the nucleation and growth rates of ice crystals on the surface. The layered structure and concept of the photothermal trap coating are illustrated in Figure 1.1.

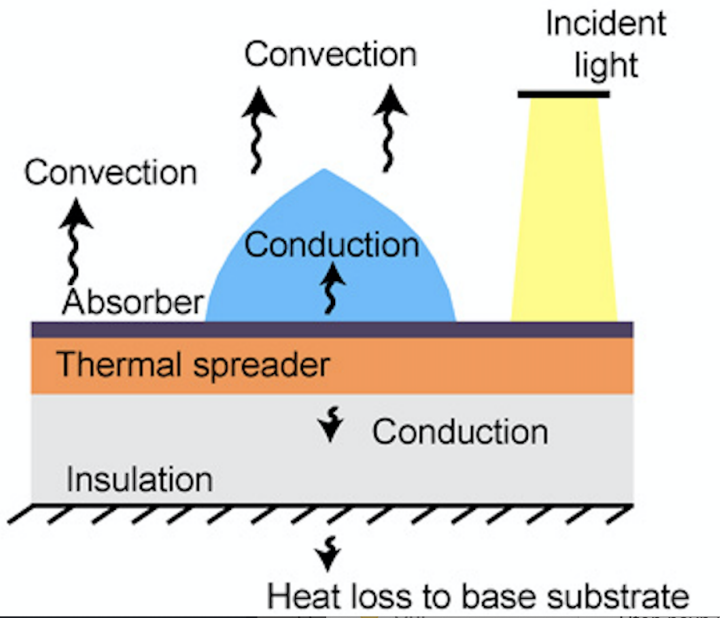

Figure 1.1: Schematic illustrating the structure and concept of the photothermal trap coating. Arrows represent the heat transfer in the system. The thickness of the layers are not to scale. (From Science Advances© Dash, de Rutier, Varanasi [2], some rights reserved; exclusive licensee American Association for the Advancement of Science. Distributed under a Creative Commons Attribution NonCommercial License 4.0 (CC BY-NC) http://creativecommons.org/licenses/by-nc/4.0/)

The effectiveness of the photothermal trap is determined by two factors: The temperature increase on the surface in response to illumination, and the thermal response time. These factors can both be tuned by the choice of materials for each of the three coating layers.

For the top layer of the trap, it is suggested that a selective absorber material be used. Such materials absorb a major fraction of incoming radiation and converts it to

thermal energy, rather than reflecting or re-emitting it. For the heat to be transferred to the second layer of the coating, this absorber material also has to have a fairly high thermal conductivity. Furthermore, the surface structure and wetting properties of this layer are important to consider, seeing as these greatly affect how ice adheres to the coating. Below the absorber, there is a thermal spreader layer, which function is to spread the heat along the coating plane. This is a crucial factor for the de-icing properties of the coating, as the surface is unable to absorb radiation in spots where ice has already accumulated. Heat must consequently be transported here from illuminated areas of the coating. The primary criteria when choosing the material for this middle layer is therefore a high thermal conductivity. Finally, there should be a thermally insulating layer below the thermal spreader to restrict heat loss to the substrate.

Dash et al. had great success in the testing of their prototype for this coating [2]. They recorded an increase in surface temperature of up to 33 °C upon solar illumination, which shows that this type of coating could be a highly efficient approach to dealing with surface icing. However, the details on which material is being used as the selective absorber layer is not disclosed.

1.3 Aim of the work

The main objective of this Master's Thesis is to prepare and characterise four prototypes of a photothermal trap coating designed for de-icing purposes. The coating will utilise heat generated from photothermal conversion of solar illumination to melt off ice deposited on the surface. The thesis is an extension of the work performed by the author in the specialisation project [18].

All three layers of the photothermal trap coating are important to the de-icing function, but the properties of the selective absorber are the most complex and interesting. In this study, prototypes of the photothermal trap coating with four different absorber materials are prepared by tape casting of ceramic slurries onto strips of aluminium foil. The coating surfaces are then characterised by scanning electron microscopy (SEM) and stylus profilometry. Their wetting behaviour is characterised by water contact angle (WCA) measurements, and their hardness and durability by scratch testing. The de-icing abilities of each prototype coating are evaluated using a simple experimental setup. The optical properties of the four absorber materials are characterised by integrating sphere spectroscopy, and the thermal properties by differential scanning calorimetry (DSC) and laser-flash methods.

The results from the characterisation are used both to review the four materials as selective absorbers for this type of de-icing coating, and to review the method of coating preparation.

2 Theory

2.1 Introduction to surface icing

Icing on a surface can be caused by various atmospheric phenomena, and is usually categorised as either in-cloud icing, precipitation icing, sea water icing or frost. Each of these will be reviewed in this section, and photographs showing how they differ in appearance are given in Figure 2.1. Ice that is formed under natural conditions is a stochastic substance where water molecules are held together by hydrogen bonds. Even though the molecules always arrange themselves on a hexagonal crystal lattice, the disorder of their direction causes each case of icing to be somewhat unique [19].

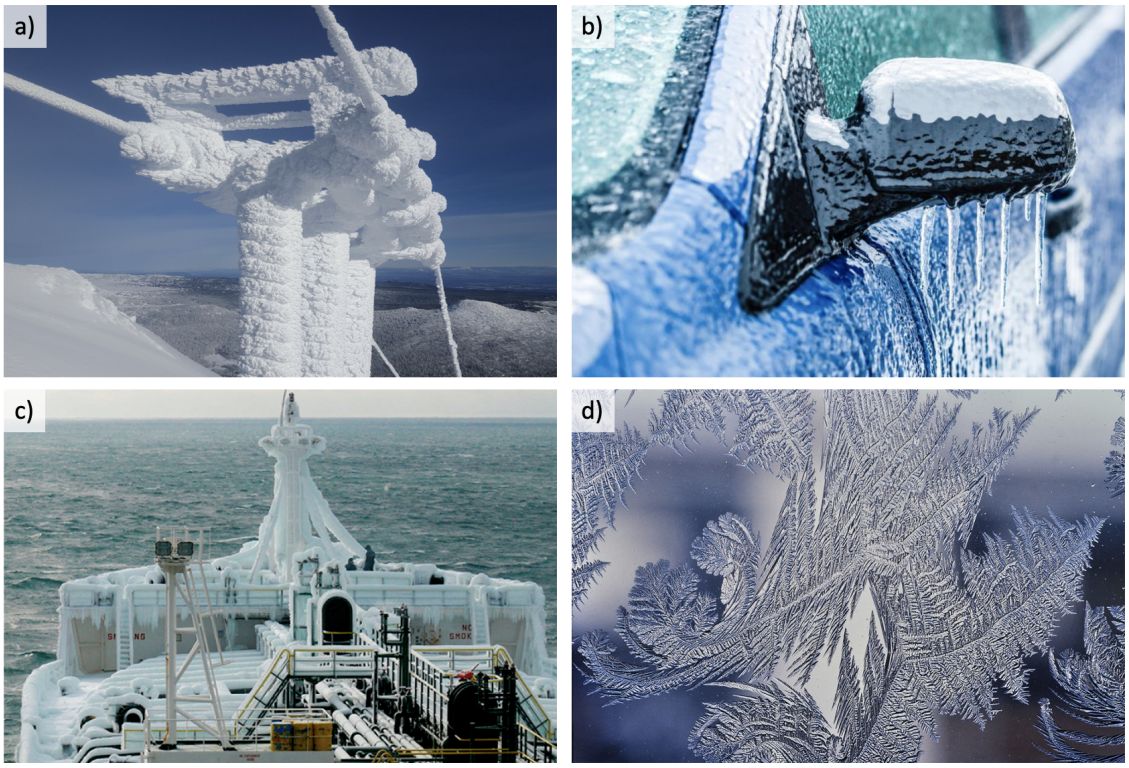

Figure 2.1: Photographs showing examples of a)rime ice formed from in-cloud icing, b) precipitation icing caused by freezing rain, c) sea water icing, and d) frost ice. The images are adapted from [20], [21], [22] and [23].

In-cloud icing (Figure 2.1a) occurs when tiny, supercooled water droplets in a cloud or fog impacts on a surface in conditions below 0 °C (sub-zero), causing the droplets to instantly freeze onto the surface. Depending on the weather situation and cloud characteristics, the resulting rime ice may be either hard or soft in texture. Since the conditions necessary for in-cloud icing to occur are rather rare, it is mostly seen on structures located in elevated and exposed terrain [7].

Precipitation icing (Figure 2.1b), on the other hand, can occur on all surfaces that are exposed to a combination of sub-zero conditions and some kind of precipitation. Both the properties and appearance of the accumulating ice is greatly affected by the nature of the precipitation. Depending on the vertical temperature distribution of the lower atmosphere this may be in the form of freezing rain, wet snow, dry snow, or anything in between. Dry snow poses less problems than wet snow and freezing rain, as the latter two form ice that is more dense and has a higher surface adhesion [1, 7]. Ice accretion in marine climates can sometimes be a result of supercooled sea water being sprayed or blown onto a cold surface (Figure 2.1c) [22].

All the aforementioned icing processes are due to a phase transition from liquid to solid water. Frost ice, on the other hand, is a state that is formed when water vapour transitions directly to solid ice on sub-zero surfaces (Figure 2.1d) [7]. This phase transition is often referred to as desublimation, and is the same transition that takes place in the atmosphere in the creation of snowflakes [19]. This allows for more crystalline microstructure than other types of surface icing, and an order similar to the characteristic six-fold symmetry of snowflakes is often observed in frost ice as well.

2.1.1 Ice adhesion

The adhesion between a surface and the ice that is accumulated on it can be described by a set of forces acting at the interface [19]. Firstly, chemical bonds are formed between the molecules on opposite sides of the interface. This lead to a short range attractive force that, depending on the chemistry of the surface and its affinity to water molecules, can be strong or weak. Secondly, there are electrostatic interactions that arise from non-compensated spatial charge distributions in both the substrate and the ice. Opposite charges at their respective surfaces then result in a strong, attractive force at the interface [19]. Finally, as for any intermolecular action, van der Waals forces are present at the ice-surface interface as well. These are weak, attractive forces that result from the formation of temporary dipoles in the molecules and atoms at the interface [24]. Of these three, the electrostatic forces are found to have the largest contribution to the total adhesion [19, 25].

Ice adhesion is very complex, and there is yet to be found a single model that can be used to adequately predict how strong it is for a given icing system [14, 24, 26, 27]. The strength of ice adhesion relies on many different parameters, related to both the surface and type of ice. As discussed earlier, the nature of accumulated ice on a surface can vary a lot depending on the conditions it was formed in. A recent study performed by Rønneberg et al. suggested that ice adhesion strength decreases with increasing density of the deposited ice [15].

When it comes to the surface the ice adheres to, its wetting properties are usually looked at as a contributing factor. Although there is still an ongoing discussion about whether there is a correlation between hydrophobicity and low ice adhesion strength [11, 12], it is still the main focus of anti-icing research. Surface wetting properties are further discussed in Section 2.2. Furthermore, it is not only important to consider the chemistry of the surface, but also the physical structure. A rougher surface has been shown to give stronger ice adhesion, for samples with the same chemical composition, and this is mostly likely attributed to frictional forces at the interface [28–30].

In general, ice adhesion strength is defined as the force needed to remove the ice from the surface, divided by the area of ice-surface interface [11]. Various research groups working on this topic are operating with very different methods of measuring this, and especially in regards to the ice removal strategy, which can be either by a shear, tensile or centrifugal force [31]. Moreover, the method used to deposit ice onto the surface varies a lot between individual studies as well. In particular, it has been shown that the use of impact ice (simulating precipitation icing) vs. non-impact ice (simulating in-cloud icing) gives significantly dissimilar results [32]. Due to these measurement differences, there is low accuracy in comparing the results of separate studies that have measured ice adhesion strength.

2.2 Solid surface wetting

As previously mentioned, the wetting interaction between the surface and incident water droplets is one of the most important factors of icing, particularly of precipitation icing. When a droplet is deposited on a flat surface, gravitational forces will work to flatten it out into a thin film on the surface. Due to surface tension, a smaller surface area of the droplet is often more energetically favourable, and the liquid will in most cases take on a curved, dome-like shape. The most common parameter used when describing wetting phenomena is the contact angle, θ, which is the angle between a flat surface plane and the liquid-air interface [33, 34]. Furthermore, three cases of interfacial tensions can be defined. One between the solid surface and gas phase (γ_{sg}); one between surface and liquid phase (γ_{sl}); and one between liquid and gas phases (γ_{lg}). θ is related to γ_{sg}, γ_{sl} and γ_{lg} through Young's equation [35–37]:

$$\gamma_{sg} = \gamma_{sl} + \gamma_{lg} cos\theta \tag{2.1}$$

For water deposited on a surface, we define the surface as hydrophilic if θ < 90 °and hydrophobic if $\theta \geq 90$ °. The case of complete wetting (θ = 0 °) is mostly hypothetical, as the liquid can not spread infinitely, but the term is still used to describe surfaces with exceptionally low contact angles [34]. Materials with hydrophobic surfaces are

thoroughly researched because their water-repelling abilities have potential to be utilised in many different fields of technology. Figure 2.2 illustrates the three distinct cases of wetting on a smooth, horizontal surface.

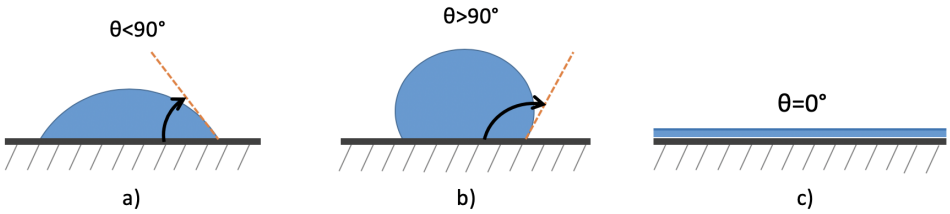

Figure 2.2: Three cases of wetting on a solid surface, where a) shows wetting on a hydrophilic surface, b) on a hydrophobic surface and c) illustrates the event of complete wetting

A droplet deposited on, or sliding down, a tilted surface will have dissimilar contact angles on the upper and lower sides, which are termed the receding (θ_r) and advancing (θ_a) contact angles, respectively. The values of these lie on either side of the apparent contact angle measured on the same surface if it was horizontal. The difference (θ_a - θ_r) is termed the contact angle hysteresis [35].

Wetting of real surfaces

All of the ideas presented thus far are based on the assumption of an ideal, smooth, surface with homogeneous chemistry. Real-life surfaces are, in most cases, chemically heterogeneous, and have some surface roughness that result in quite different wetting properties than the case described by the Young equation. The wetting of rough surfaces is usually described by one of two models [10, 38]. The first of these is the Wenzel model [39], where the open pores that are in contact with the liquid are assumed to get completely filled with said liquid. Wenzel states that, based on this assumption, the rough surface will vastly increase the area of surface-liquid interaction, resulting in the surface properties of the material being emphasised. Hence, an inherently hydrophobic material will experience even higher contact angles with increased surface roughness. This situation is described by the Wenzel equation,

$$cos\theta_{App} = r cos\theta_{Young} \tag{2.2}$$

where θ_{App} is the apparent (measured) contact angle, θ_{Young} is the Young contact angle, and r is the ratio between the true surface area in contact with the liquid and the apparent contact area [36]. The second model is the Cassie-Baxter model [40], in which the liquid does not penetrate the open pores. The liquid drop can then be described as resting on top of the roughness, making the interfacial area between the surface and liquid much smaller than in the Wenzel model. The surface properties

are then downplayed, and the interactions between the liquid and gas phases become more prominent.

In a real case of wetting on a rough surface, the situation is most likely a combination of the two models, with pores that are partly penetrated by liquid, but also contain trapped pockets of air [41]. These considerations cause the apparent contact angle of a rough surface to be very different from a contact angle measured on a smooth surface of the same material. The cases of Wenzel, Cassie-Baxter and a combination scenario are illustrated in Figure 2.3.

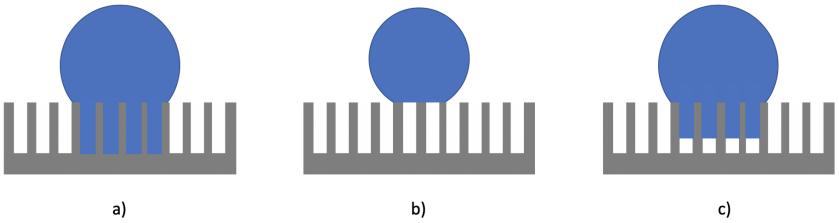

Figure 2.3: Schematic showing three scenarios of rough surface wetting: a) Wenzel state, b) Cassie-Baxter state, and c) combined Wenzel/Cassie-Baxter state

Capillary rise

Another phenomenon in wetting chemistry is the case of capillary rise. When the opening of a narrow tube, such as an open pore, is brought in contact with water, a small amount of liquid is drawn into the tube. The reason for this is that the wetting of the inner tube surface lowers the energy state of the system. A capillary pressure difference (ΔP) is established across the liquid-air interface, and this is related to the contact angle (θ), water-air interfacial tension (γ_{lg}) and tube diameter (D) through Laplace's law [35, 42],

$$\Delta P = \frac{2\gamma_{lg} cos\theta}{D} \tag{2.3}$$

Correlation to ice adhesion

Since wetting characteristics are believed to be so strongly linked to how ice adheres to a surface, this correlation has been thoroughly researched [13, 29, 43]. Generally, it is accepted that ice adhesion decreases with increasing water contact angle [7, 44]. Makkonen et al. [14] showed that the ice adhesion strength is related to water surface tension (γ_{lg}) and contact angle (θ) via the following equation, where W_A denotes the work of adhesion:

$$W_A \approx \gamma_{lg}(1 + cos\theta) \tag{2.4}$$

Surfaces characterised as icephobic (i.e. showing little to no interaction with ice) have been reported to experience a high degree of Cassie-Baxter wetting, where the small interfacial area between the ice and surface causes an overall low adhesion between the two phases [10]. It is worth noting that several additional factors usually have to be in place for a surface to behave in a truly icephobic manner, among these low water affinity, promotion of homogeneous ice nucleation and poor stability of the ice-solid interface [10].

2.3 Optical absorption and photothermal conversion

When electromagnetic radiation interacts with matter, the energy can either be absorbed into, reflected/scattered by, or transmitted through the material. How the total incident radiation distributes across these three options is the basis of how humans perceive the colour and opacity of the matter [45]. The absorption part of this equation is crucial to the function of the photothermal trap, and will therefore be reviewed in further detail in this section.

In the event that a photon (= quantum of electromagnetic radiation) collides with the atoms and molecules in a material, energy is released. If the energy of the photon is equal to or greater than the band gap of the material, this interaction can knock an electron across this band gap, into the conduction band. Since this new state is energetically unfavourable, the electron will quickly fall back into its ground state in the valence band. This fall-back releases energy in the form of either re-emitted photons, heat, or both [46]. The energy release that results in heat evolution is what is considered as absorption. The fraction of incident radiation that is absorbed by a material is termed the absorptivity. Absorptivity is not to be confused with the term absorbance, as the latter is defined as the negative natural logarithm of the transmittivity (the fraction of incident radiation that is transmitted through the material) [45].

The emissivity of a material is defined as the ratio of the radiation emitted from the material to the radiation emitted by an ideal black body at the same temperature. In an equilibrium state, the absorptivity and emissivity of a material are equal. However, if an object absorbs more radiation that it emits, then the internal temperature of the object increases and it is no longer in equilibrium with the environment [45]. In the field of solar energy this whole process where radiation is converted to heat is often called photothermal conversion [47, 48]. Efficient photothermal conversion in a material is reliant on high absorbance and low thermal emissivity [47, 49].

Photothermal characteristics can be measured using several different techniques, with variations of spectroscopy and calorimetry being the most common [48]. In photothermal lens spectroscopy, the heat development of an irradiated sample can

be measured by quantification of the photothermal lens effect that occurs. When the temperature of matter increases, its density decreases due to thermal expansion. This causes a change in the refractive index of the matter that can be observed and measured as the divergence of a laser beam shining through it [50]. This method is widely used to characterise the photothermal conversion of transparent gases and liquids.

For non-transparent material samples, the optical and thermal aspects of photothermal conversion are often measured separately, and one method of measuring the absorbance of a solid sample is by integrating sphere spectroscopy. The integrating sphere is a hollow, spherical device with a reflective, white coating on the inside. This environment allows for *diffuse* optical measurements of the sample, meaning that the spatial direction of radiation is not regarded [51, 52]. Thermal emission methods are used to measure the emissivity of solid samples. These measure the infrared radiation that is emitted by a sample as a consequence of optical absorbance [50].

2.4 Material selection for the photothermal trap coating

As mentioned in Section 1.2, the choice of materials used in a photothermal trap coating is essential to its final performance, and there are several aspects to consider in the search for possible candidates. First of all, the materials need to have the designated properties that contribute to the de-icing function of the coating. Secondly, they should have mechanical properties that ensure a long-term durability, and at the same time allow for the thin layer assembly illustrated in Figure 1.1. Finally, as for any material selection process, it is also important to look for the candidate that meets these criteria whilst being cheap, non-toxic and preferably made from abundant elements.

Solar selective absorber materials are heavily researched, due to their use in concentrating solar power systems, where incident sunlight is converted to thermal electric power [53, 54]. These can have many different compositions, structures and mechanisms of absorption. Some rely on semiconducting properties, some on microstructured surfaces, and others on a multi-layer system where radiation is reflected between the individual layers [47]. Based on the required properties, four absorber materials are proposed as possible candidates for the top layer of the photothermal trap. These, along with their key thermal and optical characteristics are presented in Table 2.1.

Table 2.1: Materials proposed for use as absorber layer in the photothermal trap coating, presented along with relevant thermal and optical properties.

Material	Chem. formula	Thermal conductivity [W/mK]	Absorbtivity [%]	Emissivity [%]
Silicon carbide	SiC	80 (hot-pressed) [46]	60 (λ=550 nm) [55]	94 [56]
Cupric oxide	CuO	33 [57]	91 [47]	19 (at 140 °C) [58]
Black nickel	Ni-Sn (alloy)	N/A	92-98 [47]	8-25 [47]
Black chrome	Cr/Cr_2O_3 (cermet)	N/A	97 [47]	9 [59]

From the information in Table 2.1, it is clear that the black nickel and black chrome absorbers would show the highest efficiency of photothermal conversion (ref. Section 2.3), closely followed by cupric oxide. Márquez et al. performed a characterisation study of cupric oxide films [60], where they concluded that the material performed well as a selective absorber. However, it is safe to assume that they all have fairly low thermal conductivities, compared to silicon carbide. The thermal conductivities of pure metal nickel and chromium are 91 W/mK [61] and 93 W/mK [62], respectively, and these would be significantly lower for an alloy or composite containing each of the metals [46]. This could impede the transfer of heat between the absorber and spreader layers of the coating. Moreover, silicon carbide is considered to be a very durable material, with a remarkable hardness and resistivity to acidic corrosion [63]. It is also a cheaper and more accessible material than both black chrome and black nickel [56, 64, 65]. It is worth exploring whether the thermal conductivity of cupric oxide could be increased by using it in a ceramic-metal composite (cermet) with metallic copper.

Table 2.2 presents three alternative materials that could be used as the spreader layer of the photothermal trap coating. Even though aluminium has the lowest thermal conductivity of the three, it is considered to be the preferred alternative as it is cheap, lightweight, non-toxic and easily available [66]. Aluminium metal is, in fact, about a hundred times cheaper than pure silver metal [46]. Metallic copper would also be a reasonably good candidate as it is an excellent thermal conductor, and has a price point comparable to that of aluminium. However, it has more than twice the specific mass of aluminium [46], and is reported to have some unfortunate toxic effects [67, 68].

Table 2.2: Metals proposed for use as the thermal spreader layer in a photothermal trap coating, and each of their thermal conductivities.

Material	Chem. formula	Thermal conductivity [W/mK]
Aluminium	Al	222 [69]
Copper	Cu	400 [57]
Silver	Ag	428 [46]

When it comes to the innermost layer of the coating, the most important factors are that this material has a low thermal conductivity and allows for satisfactory adhesion to the substrate. This criteria is met by a number of different materials, so a cheap and easy solution would be to use some kind of commercially available, insulating foam.

2.5 Methods of de-icing characterisation

There is, to the authors best knowledge, no existing standard experimental setup that can be used to to characterise the performance of potential anti- and de-icing coatings. When considering that illumination needs to be included as a variable, the characterisation method is further complicated. Dash et al. [2] studied the de-icing effects of their photothermal trap coating using a specifically designed cold chamber equipped with a side view port. With this device, they managed to keep stable, cold conditions inside the sample chamber while the sample surface was recorded through the port. A halogen fibre light with low thermal radiation (max. 1.8 kW/m^2) was used to simulate sunlight. This characterisation setup is both complex and expensive, and the following paragraphs look into other alternatives for performing these kinds of measurements.

Former NTNU Master Student Raasok wrote their thesis on hydrophobic anti-icing coatings in 2014 [70], where a fairly simple setup was used to study icing characteristics. The coating samples were mounted with tape to a 45°inclined aluminium plate which was then cooled to sub-zero temperature in a walk-in freezer. Precipitation icing was emulated by spraying finely dispersed ice water onto the freezing surface of the coating sample. The freezing-, and subsequent melting behaviours on the surface were then observed closely. Raasok reports that this setup was inspired by the experiments performed in anti-icing studies by Lee et al. [71] and Cao et al. [72].

The method used in Raasok's study would have to be modified in order to characterise the de-icing ability of a photothermal trap coating, seeing as the illumination variable is so important. To fully observe how illumination affects the de-icing process, two parallels of the experiment are necessary. One where the sample surface is illuminated; and one where it is not. During the specialisation project by the author [18], de-icing characterisation was performed by a modified version of Raasok's method. Two parallels of samples were mounted on the aluminium plate to be characterised simultaneously. After the ice had been deposited, the plate was brought out to room temperature, and the de-icing process observed. One of the parallels was illuminated using a 1050 lm light bulb, while the other was covered up by a light-safe chamber until the very end of the experiment.

There are three main challenges to consider in the further development of this characterisation method. The first one is that all variables except for the presence of illumination should be kept constant for both parallels. This includes constant temperature, humidity and air flow in the environment surrounding the samples. It is safe to assume that a light-safe chamber, such as the one used in the specialisation project [18], does not ensure this. The second challenge is with recording the de-icing progress of unilluminated samples. To make visual observations, or record results with a camera throughout the experiment, the sample surface needs to be illuminated. This will disturb the process, and can have a significant effect on the results of the characterisation. The third, and final, challenge of this characterisation is with observing the actual melting of the ice on the sample surface. The droplets that are deposited freeze into a very transparent type of ice that makes it hard to determine the rate of melting throughout the experiment.

3 Experimental

Figure 3.1 presents an overview of the experimental work. The procedure is based on the work performed by the author in the specialisation project [18], with some modifications and additional steps. Two kinds of samples were primarily prepared. The first kind are a set of prototype coatings used to characterise surface properties, durability and de-icing properties of the prototype coatings. The other kind are pressed powder pellets prepared in order to characterise the optical and thermal properties of the potential absorber materials.

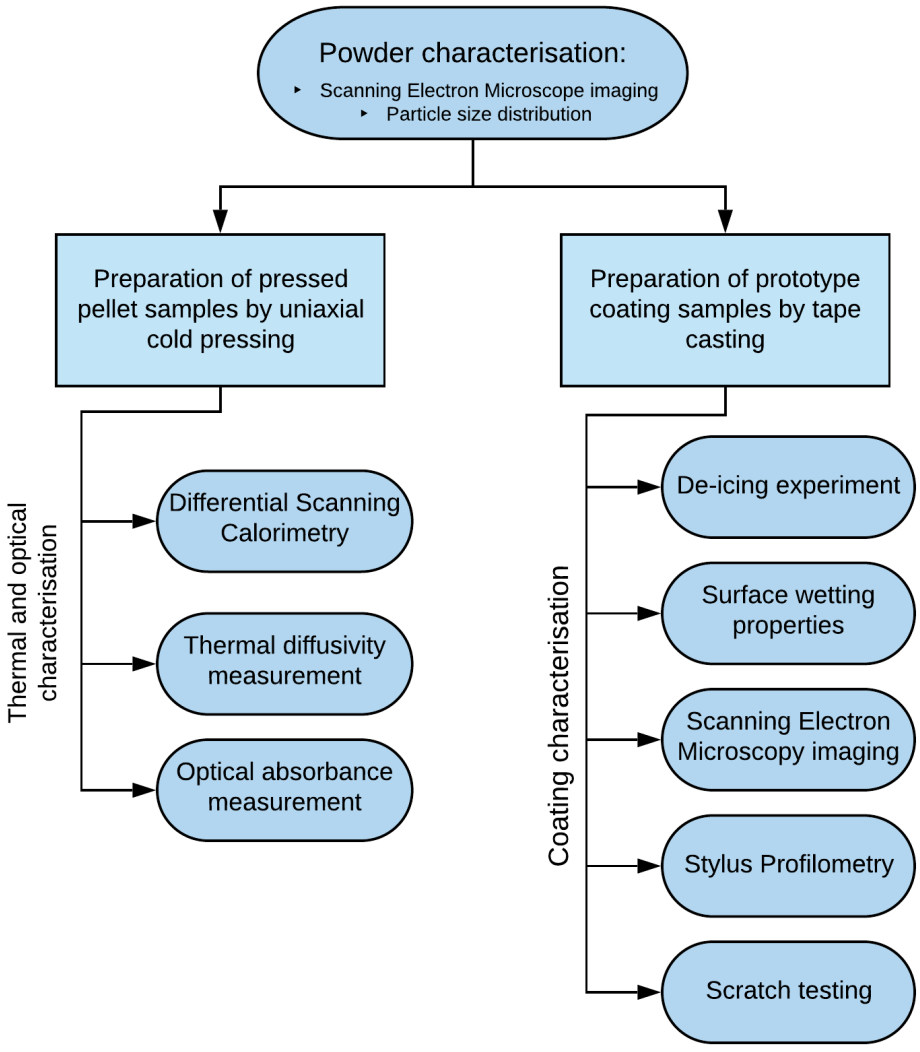

Figure 3.1: Flowchart presenting an overview of the experimental work that was performed in this Master's Thesis.

3.1 Chemicals

Table 3.1 lists the chemicals used to prepare the samples for the experimental work of this master's thesis. This table also provides supplier data, purity and average particle size of the chemicals, where these are known.

Table 3.1: Overview of the chemicals used in the experimental procedure.

Chemical	Formula	Function	Distributor	Purity [%]	CAS number
Silicon carbide	SiC	Ceramic powder	Saint Gobain	N/A	N/A
Copper	Cu	Metallic powder	Alfa Aesar	≥99	7440-50-8
Cupric oxide	CuO	Ceramic powder	Sigma Aldrich	≥99.9	1317-38-0
Polyvinyl butyral (PVB)	$(C_8H_{14}O_2)_n$	Binder	Sigma Aldrich	N/A	63148-65-2
Ethanol	C_2H_5OH	Solvent	VWR	≥ 96	64-17-5

3.2 Sample preparation

Samples of four different absorber materials were prepared and characterised. They contain the following ratios of ceramic and metal components:

- **SiC** samples contain spray-dried silicon carbide powder.
- **30/70 Cu/CuO** samples contain a powder mixture with 30 mol% metallic copper and 70 mol% copper(II)oxide.
- **50/50 Cu/CuO** samples contain a powder mixture with 50 mol% metallic copper and 50 mol% copper(II)oxide
- **70/30 Cu/CuO** samples contain a powder mixture with 70 mol% metallic copper and 30 mol% copper(II)oxide

From this point on in this thesis, these four materials are referred to by the names given i bold.

Coating prototype samples

Coating prototypes with each of the absorber materials were prepared by tape casting ceramic slurries onto strips of aluminium foil. Tables 3.2, 3.3, 3.4 and 3.5 give the amounts of the various components in the slurries prepared for the SiC, 30/70 Cu/CuO, 50/50 Cu/CuO and 70/30 Cu/CuO samples, respectively. The following section describes the preparation of these slurries and the following tape casting procedure. Polyvinyl butyral (PVB) is used as binder as it is not soluble in water, but is readily solved in an ethanol based ceramic slurry [73].

Table 3.2: Amounts and functions of the compounds added to the slurry used to prepare the SiC samples.

Function	Compound	Amount [g]
Ceramic powder	SiC	29.9995
Solvent	96 % ethanol	32.7160
Binder	Polyvinyl butyral	4.0152

Table 3.3: Amounts and functions of the compounds added to the slurry used to prepare the 30/70 Cu/CuO samples.

Function	Compound	Amount [g]
Metal powder	Cu	7.5217
Ceramic powder	CuO	22.4942
Solvent	96 % ethanol	18.2319
Binder	Polyvinyl butyral	4.0034

Table 3.4: Amounts and functions of the compounds added to the slurry used to prepare the 50/50 Cu/CuO samples.

Function	Compound	Amount [g]
Metal powder	Cu	13.355
Ceramic powder	CuO	16.709
Solvent	96 % ethanol	26.748
Binder	Polyvinyl butyral	4.006

Table 3.5: Amounts and functions of the compounds added to the slurry used to prepare the 70/30 Cu/CuO samples.

Function	Compound	Amount
Metal powder	Cu	19.5289
Ceramic powder	CuO	10.6876
Solvent	96 % ethanol	20.6318
Binder	Polyvinyl butyral	4.0536

Starting off, a 250 ml plastic bottle was filled 1/3 of the way with milling media. For this work, 5mm zirconium oxide (ZrO_2) spheres were used as the milling media. Then, the binder was weighed out and dissolved in 10 g of the ethanol solvent before this was added to the plastic bottle. The ceramic and metallic powders were also weighed out and added to the bottle, which was then closed and shaken to start the mixing of the components. The rest of the solvent was added to the bottle, which was then sealed tight and placed on a *Tecnotest* roller mixer at 155 rpm speed for dispersion mixing overnight (~16 hours).

After dispersion mixing, the milling media was strained from the slurry using a coarsely meshed sieve. For the casting process, a *Richard E. Mistler DCX Plus* tape caster was used with the 15 cm wide reservoir. A 8 cm * 25 cm strip of aluminium foil (Unknown supplier, 0.05 mm thickness) was attached on top of the carrier film to be cast onto. The doctor blade opening was adjusted to a height of approximately 100 µm, or 50 µm above the foil. Images of this tape casting setup are presented in Figure 3.2. A small amount of slurry was then added to the reservoir and cast onto the aluminium foil at 30 % of maximum carrier speed and in room temperature environment. The tape casting process was repeated 3-4 times for each absorber material to ensure a sufficient sample quantity. The coated foil strips were left to fully dry in a fume hood overnight.

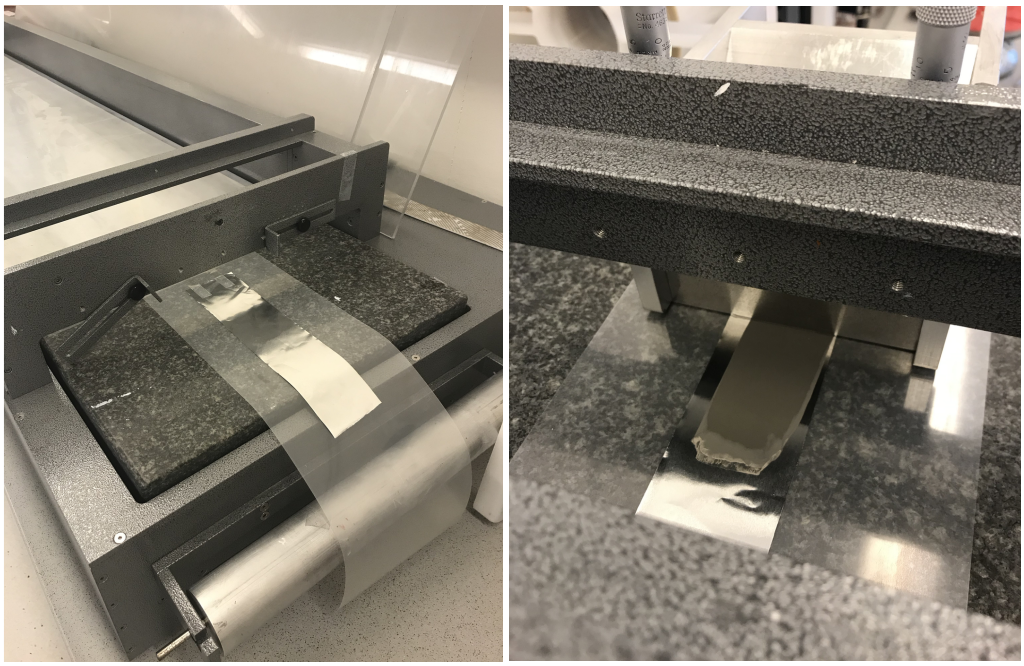

Figure 3.2: The setup for tape casting onto aluminium foil. The image on the left shows the setup of the carrier film and aluminium foil before the reservoir is put in place. The image on the right is taken from the opposite angle during the casting process.

Disc samples for photothermal measurements

The samples used to characterise the optical and thermal properties of the absorber materials were prepared separately. For all four compositions, some slurry left over from the tape casting was spread onto polymer sheets to dry. Later, the dried slurries were scraped off and ground to a fine powder using an agate mortar and pestle. Using a hydraulic, uniaxial c-press, these powders were then pressed into pellets of two different diameters, giving eight pellets in total. Table 3.6 gives the dimensions and weights of the produced pellet samples.

Table 3.6: Overview of the dimensions of the pressed pellet samples prepared in order to characterise the optical and thermal properties of the four absorber materials.

Material	Diameter [mm]	Thickness [mm]	Mass [g]
SiC	10	5.17	0.760
	15	3.75	2.438
30/70 Cu/CuO	10	4.93	1.368
	15	4.19	4.343
50/50 Cu/CuO	10	4.85	1.257
	15	4.04	4.255
70/30 Cu/CuO	10	5.10	1.378
	15	4.86	3.575

3.3 Powder characterisation

Scanning Electron Microscopy

The morphologies of the Cu and CuO powders were investigated using the scanning electron microscope (SEM) *Hitachi S3400-N* with a secondary electron detector. The samples were prepared by adhering a small piece of carbon tape to a SEM sample stub, sprinkling a small amount of powder onto the tape and removing any excess using pressurised air. An accelerating voltage of 10.0 kV and working distance of approximately 6 mm were used to achieve the desired images. The vacuum in the chamber was reported to be <1 Pa.

Particle Size distribution

The particle size distributions (PSD) of the Cu and CuO powders were determined using a *Partica LA-960* from Horiba. Distilled water was circulated through the instrument, and a background scan measured. Powder was then slowly added to the circulating water until the laser transmittance entered a range suitable for measurements. Mechanical stirring, as well as 1 minute of ultrasonic agitation, was applied in order to break soft agglomerates. Three measurements were run for each of the two powders to ensure consistent results.

3.4 Coating characterisation

Wetting characteristics

Suitable samples from each of the four prototype coatings were prepared by cutting out 1 cm * 4 cm strips of the coated foils. The wetting properties of the coating surfaces were characterised using a *Krüss Drop Shape Analyser - DSA100* with the software Krüss ADVANCE in Sessile Drop mode.

The samples were first, one by one, mounted in the associated temperature chamber TC40. The chamber was connected to a *Julabo F12-MA* refrigerated circulator, used in order to reach temperatures below room temperature. First, the chamber temperature was lowered to achieve a measured sample surface temperature of 5 °C. 2.0 µL room tempered water droplets were deposited on the surfaces at a rate of 0.16 mL/min. The contact angles were measured a total of 10 times with 5 s intervals, the first measurement done immediately after droplet deposition. The Ellipse(Tangent-1) fitting mode was used to compute the contact angles from the detected data. This procedure was repeated for sample surface temperatures 0 °C and -5 °C. Three droplets were deposited on separate sites of the surface and measured at each of the three temperatures, to ensure consistent results.

Coating samples of the same dimensions were also used to measure the advancing and receding water contact angles of the surfaces at room temperature. These samples were mounted on the instrument default stage. 2.0 µL water droplets were deposited on the surfaces at a rate of 0.16 mL/min. After deposition, the stage was tilted to a vertical position, or 90°angle. The contact angles were measured immediately after deposition and at every 5°interval of tilting up to 90°. These measurements were repeated for three separate droplets on each of the four absorber material surfaces, to ensure consistent results.

Mechanical properties

1 cm * 4 cm strip samples were cut from each of the four prototype coating foils and taped onto a 3 cm * 5 cm steel plate substrate (Steel St52), before the mechanical hardness of these samples were tested using an *Anton Paar Micro Scratch Test* instrument. An indenter tip was lowered onto the sample surface and applied a given downward force, and the penetration depth of this tip into the sample was simultaneously measured. The diamond indenter has a diameter of 200 µm. For these measurements, progressive scratch programmes were run, meaning that the tip was dragged along the surface and applied a linearly increasing force. Two such measurements were run for each sample, on different sites of the sample surface. Table 3.7 shows the specific details for the parameters used to characterise each sample. The associated optical microscope was used to study the features of the resulting scratches, and determine the point of breach for the absorber material layers.

Table 3.7: Scratch parameters used in the mechanical testing of the prototype coatings. $F_{initial}$ and $F_{terminal}$ denote the force that was applied on the indenter at the beginning and end points of the scratch test, respectively.

Sample	Scratch length [mm]	$F_{initial}$ [mN]	$F_{terminal}$ [mN]
SiC	3	30	10 000
30/70 Cu/CuO	3	30	5 000
50/50 Cu/CuO	3	30	10 000
70/30 Cu/CuO	5	30	15 000

Surface profile

1 cm * 4 cm strip samples were cut from each of the four prototype coatings prepared in section 3.2 and taped onto a steel substrate. The surface profile of these samples were then characterised using the *Veeco DEKTAK 150* stylus profilometer located in Norfab's cleanroom facilities at NTNU. A stylus is dragged across the surface of the sample with an applied force of 3 mg, detecting the vertical displacement from a baseline height. Three scans of 15 mm were run for each material, detecting both hills and valleys with a vertical measurement range of 524 µm. The duration of the scan programme was set to 180 s, giving a vertical resolution of 278 nm for the measurements. In order to calculate the roughness, 3 mm regions with no effects from waviness (larger-scale topological features) were studied. These calculations are further explained in Appendix A.

Surface and cross-section imaging

The surfaces and cross-sections of the four prototype coatings were imaged using the scanning electron microscope (SEM) *Hitachi S3400-N*. The surface samples were prepared by cutting 1 cm * 1 cm pieces from the prototype coatings and adhering these flat to a regular sample stub using carbon tape. The cross-section samples were prepared by separating the absorber material layer from the Al foil, and adhering the former to a sample stub designed for cross-section studies. Secondary images of both kinds of samples were achieved using an accelerating voltage of 15.0 kV and a working distance of approximately 6 mm. Additionally, the cross-section samples were imaged and elementary mapped by energy-dispersive x-ray spectroscopy (EDS) using the backscattered electron detector. For these measurements, the accelerating voltage was increased to 20.0 kV and the working distance set to 10 mm. The vacuum in the chamber was reported to be < 1 Pa for all imaging.

3.5 De-icing characterisation

The de-icing properties of the prototype coatings were investigated using a simple setup that is based on a similar experiment performed by the author in the specialisation project [18]. Two rounds of experiments were carried out. The first one to compare the properties between the three Cu/CuO compositions; the second one to compare the properties of the SiC and 50/50 Cu/CuO absorbers. The setups and procedures for the two rounds were somewhat different, and are described in the following subsections.

Comparison of the three Cu/CuO coatings

Two 1 cm * 2 cm samples were cut from each of the three Cu/CuO prototype coatings, and mounted on a custom-made, 45°inclined Aluminium plate using Scotch double-sided foam tape. Uncoated aluminium foil pieces of the same size were also adhered in the same fashion, and used as reference samples. As shown in Figures 3.3 and 3.4, the samples were arranged in two rows. One row of samples were placed at the top of the plate; and one halfway up the plate.

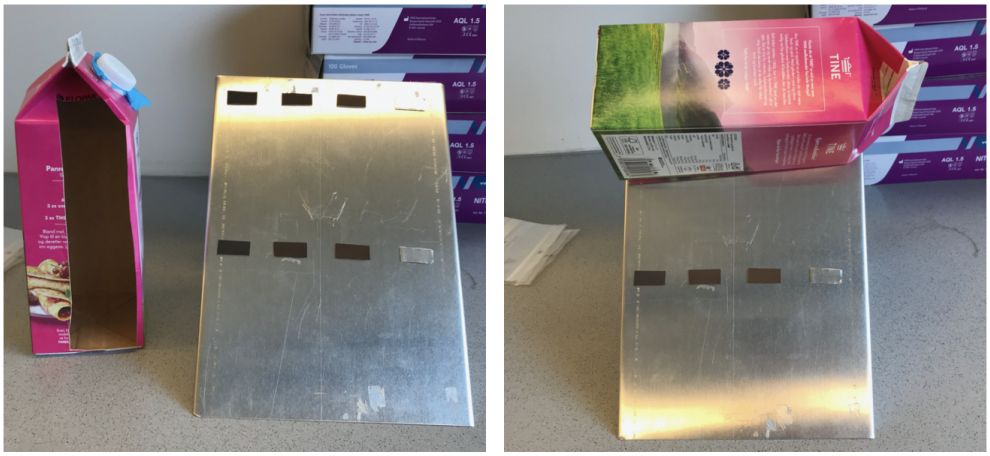

Figure 3.3: Part of the setup used to characterise the de-icing properties of the three Cu/CuO coatings.

This plate was then placed in a -20 °C walk-in freezer to achieve sufficiently cold surface temperatures. After two hours, iced water (0 °C) was deposited on the sample surfaces to simulate precipitation. This was achieved using a spray bottle at high dispersion, and from a distance of 10 cm. Twenty minutes later, images of all eight samples were captured to document the surface icing. A modified milk carton was placed over the top row of samples to create a dark environment, as demonstrated in Figure 3.3. The plate was transferred from the freezer to a 20 °C environment and the second row of samples were immediately illuminated with a 1050 lm LED light bulb from a distance of approximately 40 cm. The illuminated sample surfaces was continuously observed, and images were captured 1, 2, 3, 4, 5, 6, 7, 8, 9, 10, 15, 20, 25 and 35 min after the plate was brought out of the freezer. At the 15, 20, 25 and 35 min marks, the carton was lifted to also observe and capture images of the samples that were not illuminated.

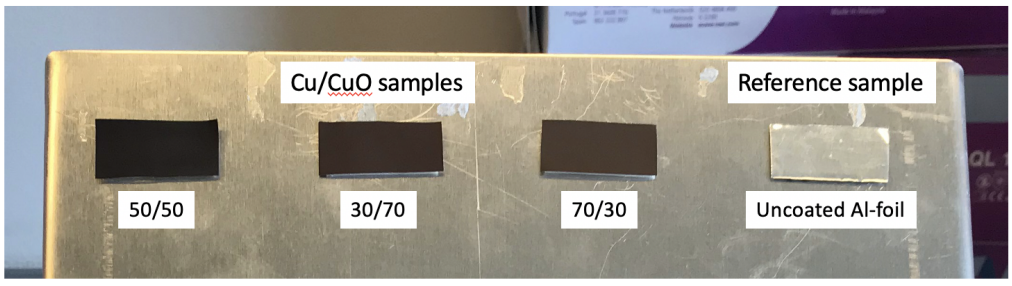

Figure 3.4: A close-up image of the samples used to characterise the de-icing properties of the three Cu/CuO coatings.

Comparison of 50/50 Cu/CuO and SiC coatings

Two 1 cm * 2 cm samples were cut from both the SiC and 50/50 Cu/CuO prototype coatings, to be mounted on the custom-made, 45°inclined Aluminium plate using Scotch double-sided foam tape. An uncoated aluminium foil piece of the same size was also adhered in the same fashion, to serve as a reference sample. A close-up image of these samples is shown in Figure 3.5.

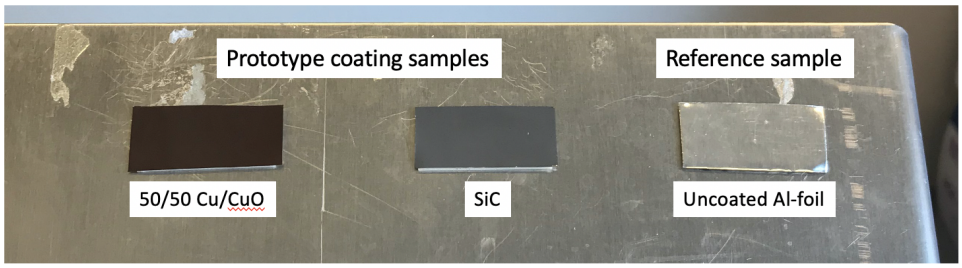

Figure 3.5: A close-up image of the samples used to compare the de-icing properties of the SiC and 50/50 Cu/CuO prototype coatings.

As for the previous experiment, the aluminium plate was placed in a -20 °C walk-in freezer for two hours before iced water was deposited on the sample surfaces. Twenty minutes later, images of the three samples were captured to document the surface icing. The plate was transferred to a Styrofoam box outside of the freezer, together with cooling elements and a thermometer sensor. This setup is demonstrated in Figure 3.6. At 1, 3, 5, 7, 10, 15, 20, 25, 30, 35, 40, 45, 50, and 60 minutes after transfer, images of the samples were recorded to observe the de-icing development. The temperature inside the box was also measured at each of these time stamps. Outside of these brief moments, the lid of the Styrofoam box was kept shut to keep a dark environment and stable temperature.

Figure 3.6: Pictures presenting the setup and the Styrofoam box used when comparing the de-icing properties of the 50/50 Cu/CuO and SiC prototype coatings.

This whole procedure was later repeated, but this time with a 1050 lm light bulb mounted on the inside of the Styrofoam box lid, illuminating the samples from a distance of approximately 10 cm. To ensure a fair comparison with the unilluminated parallel, the Styrofoam lid was opened to make observations and capture images at equivalent time stamps. This experiment was however terminated 35 minutes after the transfer to the Styrofoam box, at which point there was no longer any changes to be observed on the sample surfaces.

3.6 Optical and thermal characterisation

In addition to the characterisation of the prototype coatings, optical and thermal properties of the four absorber materials were characterised.

Absorbance

Absorbance data for the four material compositions at room temperature were acquired using an *Avantes* integrating sphere. The measurements were run by PhD candidate Håvard Wilson at the Department of Materials Science and Engineering, NTNU. A scan with no illumination was run to obtain a "dark spectra", which is used to get rid of any background noise. Next, a reference spectra was obtained by running an illuminated scan on an aluminium foil sample with high reflectance. The light source used is a *Newport* 300 W Xenon arc lamp, and the measurement was run for light in the wavelengths range 300-1000 nm. Then, the 10 mm diameter pressed pellet samples were, one by one, placed in the chamber and irradiated with light in the same range of wavelengths as the reference. The absorbance data was received and processed by an *AvaSpec-2048* spectrometer. For all measurements, the integration time was set to 400.000 ms, and the final data gives an average of 100 such measurements. The resulting absorbance spectra were achieved by subtracting the reflectance data of the samples from the reflectance of the aluminium foil.

Thermal diffusivity

Thermal diffusivity at room temperature for all four absorber materials were measured using the laser flash instrument *Netzsch LFA457 Microflash*. The measurements were run by SINTEF Research Engineer Anne Støre. To fit in the 0.5 inch samples holder, the edges of the 15 mm pressed pellet samples were sanded down to a diameter of approximately 12.7 mm. The thickness of each sample was also reduced to approximately 2 mm, to allow for more rapid analyses. Both of the flat sides of the samples were then spray coated with a thin layer of graphite (Graphit 33, Kontakt Chemie). To measure the diffusivity, the samples were placed into the sample holder and one side of it was irradiated with a neodymium laser at pulse width 0.3 ms. This

caused the graphite coating to heat up, and heat was diffused through the sample. An indium antimonide IR-detector then measured the resulting increase in surface temperature on the opposite side of the sample. The resulting data was later processed into thermal diffusivity values. Five such measurements were carried out for each sample, in order to ensure consistent results.

Heat capacity

Some of the powder that was used to press the pellet samples was set aside in order to measure the specific heat capacities of the four absorber materials by differential scanning calorimetry (DSC). These measurements were performed by PhD candidate at NTNU, Mohammad Adnan Mostafa, on a *Netzsch DSC 214* instrument. The temperature program used had an initial temperature of 0 °C, a heating rate of 10 $^{K}/_{min}$, and a terminal temperature of 60 °C. Prior to the sample runs, this program was run on an empty aluminium crucible to collect background data. For each material to be analysed, a small amount of powder sample was added to a crucible which was then placed in the sample chamber. Table 3.8 gives an overview of the specific sample masses used for the measurements on each of the four absorber materials. The temperature program was initiated, and the heat flow measured. Three program cycles were carried out for each sample to ensure that the results and thermal history were consistent. All measurements were run in an inert N_2 atmosphere (40 mL/min gas flow), and the heat capacities were calculated with reference to a sapphire standard.

Table 3.8: Overview of the sample powder mass used in the DSC measurements for each of the four absorber materials.

Sample material	Sample mass [mg]
SiC	10.64
30/70 Cu/CuO	1.96
50/50 Cu/CuO	2.68
70/30 Cu/CuO	13.14

4 Results

This chapter presents all the important results found from the characterisations and measurements performed on the prepared samples. The first four sections present the observations and results from the characterisation of the four prototype coatings. These include the results from the de-icing, surface roughness and surface wetting characterisations, which are considered to be among the most crucial for this report. Then, there are two sections containing the results from the optical and thermal characterisations of the four absorber materials. The following subsection then presents the results from the characterisation of the Cu and CuO powders. Lastly, there is a subsection presenting the achieved densities of the absorber materials in the three different types of samples. These densities are important to consider when discussing the correlation between results obtained from the various samples.

4.1 Coating characterisation

This section opens by presenting photographs and secondary electron scanning electron microscopy (SESEM) images of the coating surfaces and cross-sections. Following this, there are separate subsections stating the results from the surface wetting, surface profile and coating hardness characterisations.

Figure 4.1 shows a photograph of the prototype coating samples that were prepared by the tape casting procedure described in Section 3.2. Overall, the method produced samples with completely opaque and continuous layers of the respective absorber materials on the aluminium foil. The layers also appeared to be very uniform in thickness, although slight irregularities were observed as they were drying. The SiC coating surface had a matte grey colour, while the other three had different shades of chocolatey brown. Increased cupric oxide content produced a darker coloured coating surface. Figure 4.2 presents close-up images of the prototype coating sample surfaces that were captured using SESEM. The individual particles on the Cu/CuO absorber surfaces were observed to be roughly spherical in shape (b-d), whereas the SiC particles had more miscellaneous shapes and sharper edges (a). From the images, the coatings seem to have had fairly broad distributions of particle sizes. However, the particles appeared to be significantly smaller on the 50/50 Cu/CuO coating (c) than on the other two Cu/CuO coatings (b,d).

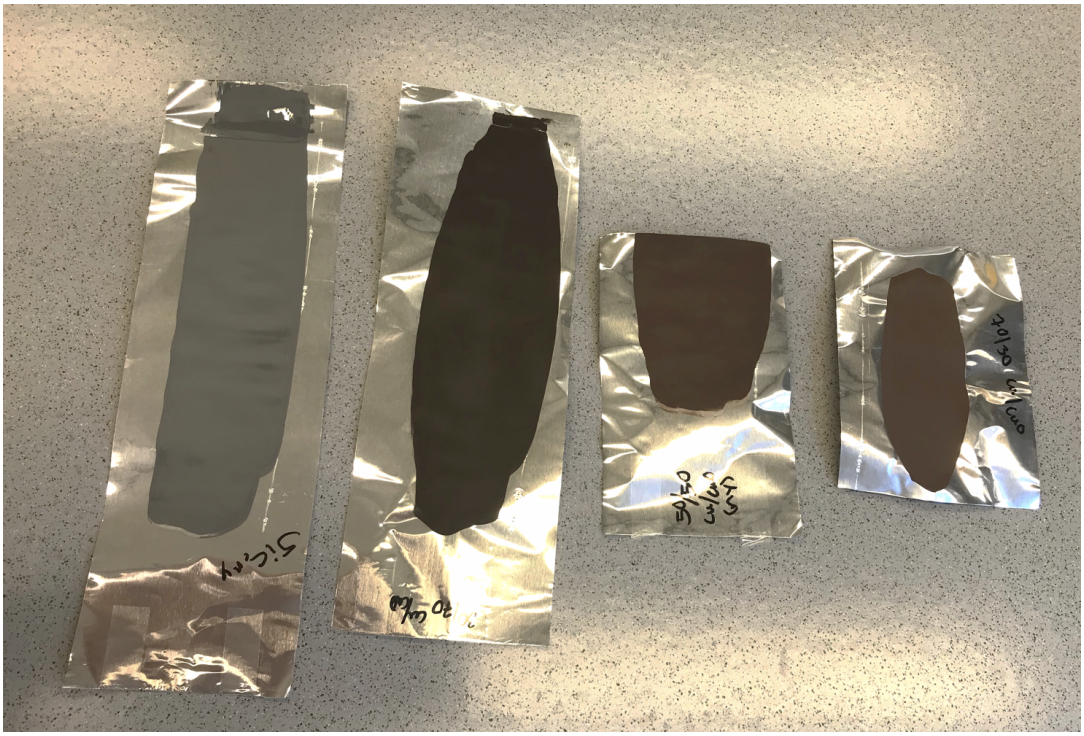

Figure 4.1: Photograph showing the prototype coating samples that were prepared by tape casting a layer of absorber material onto aluminium foil. From left to right, the samples have absorber layers made from the materials SiC, 30/70 Cu/CuO, 50/50 Cu/CuO, and 70/30 Cu/CuO.

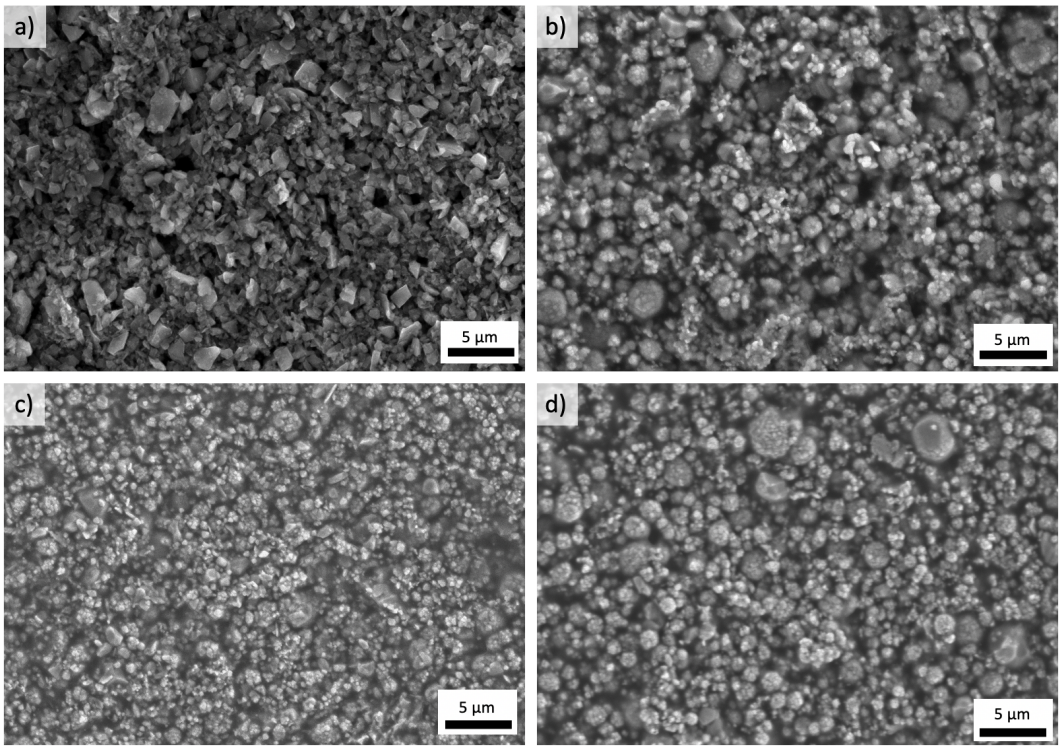

Figure 4.2: SESEM images of the prototype coating surfaces. In the four images, the surface (absorber) layers consist of the following materials: a) SiC, b) 30/70 Cu/CuO, c) 50/50 Cu/CuO, and d) 70/30 Cu/CuO.

SESEM was also used to characterise the cross-sections of the absorber layers of all four prototype coatings. Figures 4.3 and 4.4 contain SEM images of the coating cross-sections at two magnification levels, with the images of highest magnification displayed in Figure 4.4. All four coatings seemingly had rather porous inner structures, where powder particles were loosely adhered to one another via a binder matrix. The coating thickness was observed to be quite consistent within each sample. From the SEM images, the coating thickness was measured to be the following for each of the four absorber layers:

- **SiC:** 39 µm
- **30/70 Cu/CuO:** 26 µm
- **50/50 Cu/CuO:** 110 µm
- **70/30 Cu/CuO:** 46 µm

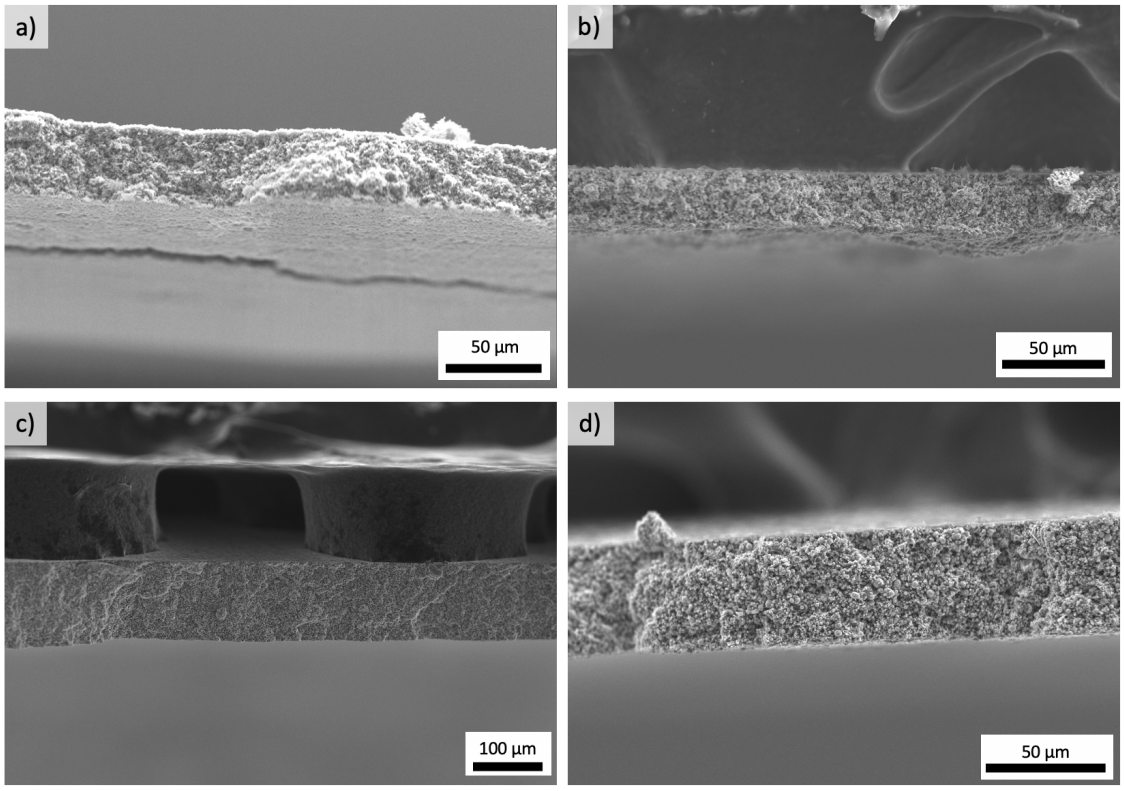

Figure 4.3: Secondary electron SEM images of the cross-sections of the absorber layers of each prototype coating. In the four images, the absorber layers consist of the following materials: a) SiC, b) 30/70 Cu/CuO, c) 50/50 Cu/CuO, and d) 70/30 Cu/CuO.

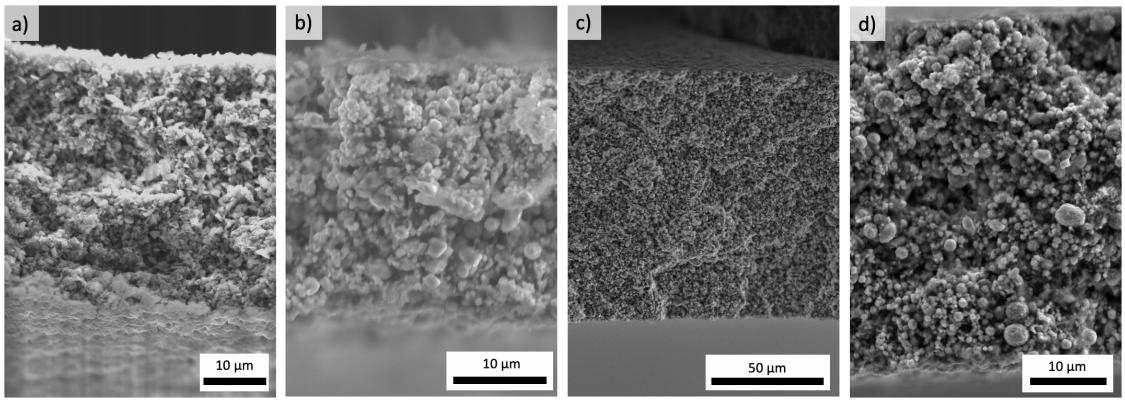

Figure 4.4: Close-up secondary electron SEM images of the cross-sections of the absorber layers of each prototype coating. In the four images, the absorber layers consist of the following materials: a) SiC, b) 30/70 Cu/CuO, c) 50/50 Cu/CuO, and d) 70/30 Cu/CuO.

The results from the energy dispersive x-ray spectroscopy revealed that there was an even distribution of the metallic and ceramic components across the cross-section of all three Cu/CuO coating samples.

4.1.1 Surface roughness

A stylus profilometer was used to characterise the surface profiles of each of the four prototype coating samples. The data obtained from these measurements was used to calculate the arithmetic surface roughness (R_a) of the four coatings. The results from these calculations can be found in Table 4.1. They indicate that the coating with SiC as absorber material had a smoother surface than both the 30/70 Cu/CuO and 70/30 Cu/CuO coatings. However, the lowest value of surface roughness was measured for the 50/50 Cu/CuO coating surface.

Diagrams illustrating the various surface profiles, as well as the procedure and formula for the roughness calculations can be found in Appendix A.

Table 4.1: Arithmetical roughness(R_a) values of each of the four prototype coating systems, calculated from stylus profilometer measurements.

Absorber material	R_a [µm]
SiC	1.38 ± 0.27
30/70 Cu/CuO	2.37 ± 0.15
50/50 Cu/CuO	0.816 ± 0.059
70/30 Cu/CuO	2.27 ± 0.23

4.1.2 Surface wetting

The diagrams in Figure 4.5 show the development of the mean water contact angles on each of the coating prototype surfaces in the first 45 seconds after droplet deposition, at three different surface temperatures. These clearly indicate that the water contact angles (WCA) were generally high and very stable over time on the three Cu/CuO cermet surfaces. At a surface temperature of 5 °C, all three of these samples could be defined as hydrophobic, and the 50/50 Cu/CuO sample was hydrophobic at every measured surface temperature. For the SiC surface, on the other hand, the water contact angles were initially quite high, but they quickly decreased.

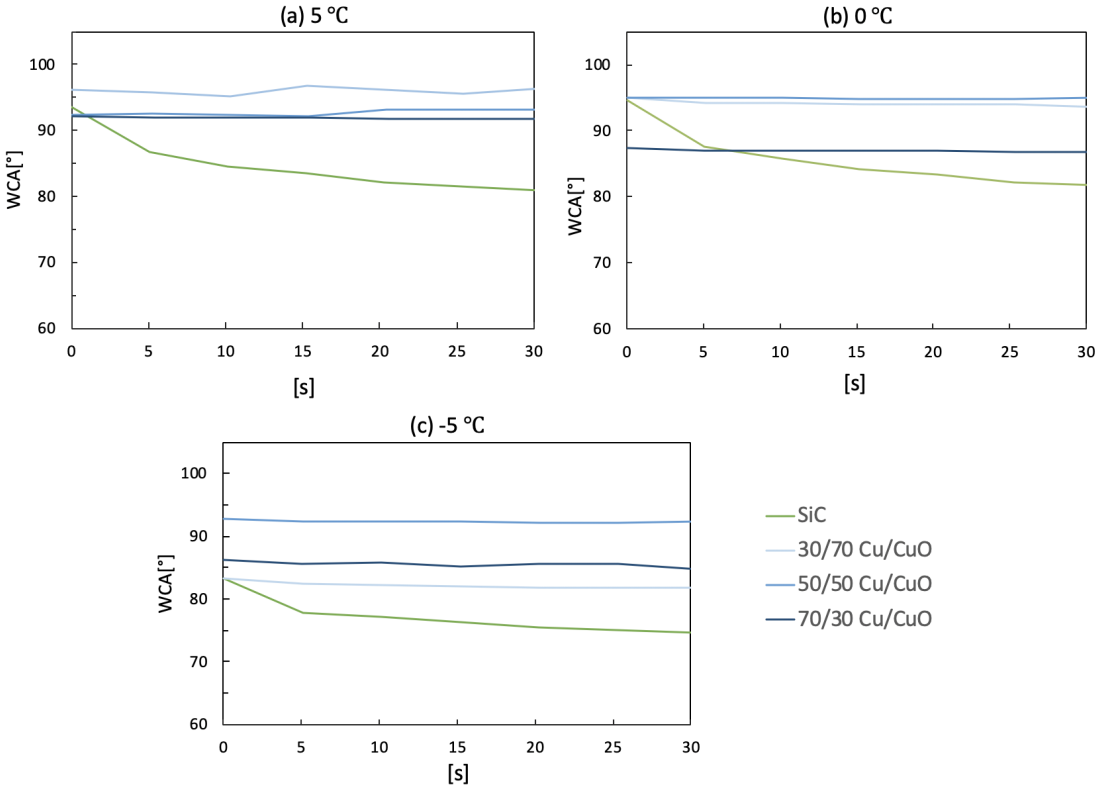

Figure 4.5: The development of the mean water contact angles of droplets deposited on each of the four coating prototype sample surfaces in the first 30 seconds after deposition, at a surface temperature of approximately a) 5 °C, b) 0 °C, and c) -5 °C.

In Figure 4.5 a), b) and c), the measurements were carried out at sample surfaces with target temperatures of respectively 5 °C, 0 °C and -5 °C. In reality, the surface temperatures fluctuated over the course of the measurements, and Table 4.2 shows an overview of the average measured surface temperatures at each target temperature for each of the four samples.

Table 4.2: An overview of the average measured surface temperatures on each of the four types of coating prototype samples, for each target surface temperature.

Target temperature [°C]	Sample material	Avg. measured temperature [°C]
5	SiC	4.8
	30/70 Cu/CuO	5.1
	50/50 Cu/CuO	5.2
	70/30 Cu/CuO	5.0
0	SiC	0.2
	30/70 Cu/CuO	-0.0
	50/50 Cu/CuO	-0.1
	70/30 Cu/CuO	-0.0
-5	SiC	-5.2
	30/70 Cu/CuO	-5.1
	50/50 Cu/CuO	-5.0
	70/30 Cu/CuO	-5.0

The wetting characterisation of tilted samples at room temperature showed that water droplets clung very well to all the absorber material surfaces. Even at a vertical stage position, the droplets did not roll or slide off any of the four sample surfaces.

4.1.3 Coating hardness

Figure 4.6 presents the results from the scratch test characterisation of the four prototype coatings as graphs where the penetration depth and measured applied force of the indenter tip are plotted as functions of the indenters position along the scratch. All of the graphs show a mostly steady increase in penetration depth with increased applied force. After the scratch tests were run, the scratches were observed with an optical microscope, and from these visual observations it could be concluded that the indenter had compressed the absorber layer progressively along the scratch. An example of this material compression, from the scratch produces on the 70/30 Cu/CuO coating sample, can be seen in the optical microscopy images in Figure 4.7 a and b. In most of the graphs, there can also be observed a steep increase in penetration depth at the very beginning of the measurement. This comes from the samples being pinned down tightly to the steel substrate by the indenter, and so the actual penetration is considered to be somewhat less deep than reported.

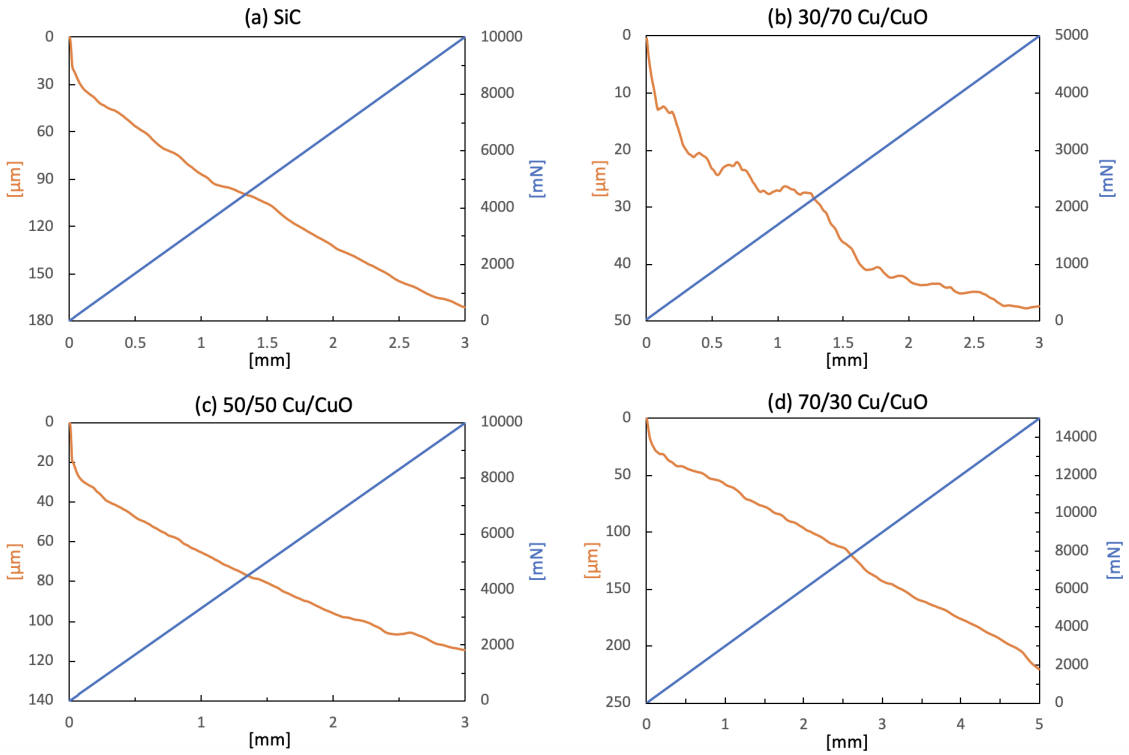

Figure 4.6: Diagrams presenting the results from the scratch test characterisation of the prototype coatings with absorber materials a) SiC, b) 30/70 Cu/CuO, c) 50/50 Cu/CuO, and d) 70/30 Cu/CuO. The penetration depth (orange) and measured applied force (blue) of the indenter tip are both plotted as functions of the indenters position along the scratch.

The visual inspection of the coatings after scratching clearly revealed the points at which each absorber layer was punctured to expose the underlying aluminium foil. Optical microscopy images from this breach of the 70/30 Cu/CuO absorber layer is shown in Figure 4.7 c and d, where the much more reflective aluminium foil is clearly revealed. These puncture points can also be identified as disturbances in the otherwise steadily increasing penetration depth graphs in Figure 4.6, and from this, the applied indenter force at the point of puncture for each coating sample were found. These values are listed in Table 4.3.

Table 4.3: Applied indenter force at the point of puncture for each coating sample

Absorber material	Indenter force [mN]
SiC	8500
30/70 Cu/CuO	2200
50/50 Cu/CuO	8800
70/30 Cu/CuO	8000

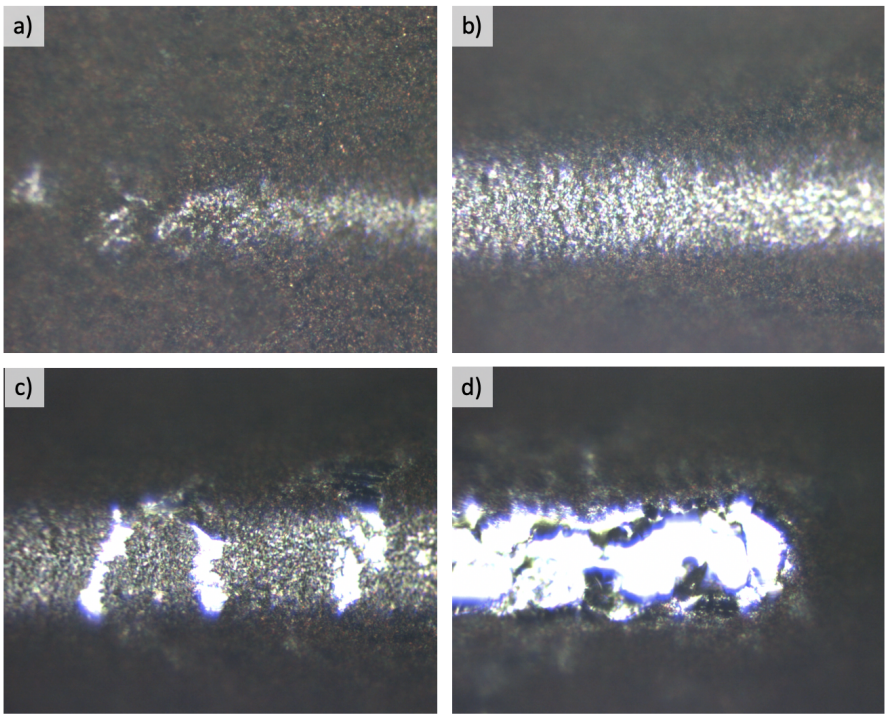

Figure 4.7: Optical microscopy images of the scratch produced on the 70/30 Cu/CuO coating prototype sample. The images show the scratch at points a) beginning, initial penetration, b) about halfway along the scratch, c) first puncture of the absorber layer, and d) end of the scratch.

4.2 De-icing characterisation

The results from the comparison of the three Cu/CuO prototype coating samples and the comparison of the 50/50 Cu/CuO and SiC coatings are presented separately. Unfortunately, the transparent nature of the deposited ice made it difficult to determine how quickly the ice melting occurred on the various sample surfaces. The observations in this section are therefore more related to the evaporation of water from the surfaces than the melting itself. The brightness and/or contrast of some photographs have been adjusted in an attempt to show the icing and wetness on the surfaces more clearly.

4.2.1 Comparison of the three Cu/CuO coatings

Figure 4.8 presents the icing and de-icing development on the surfaces of the three Cu/CuO prototype coating samples, as well as the uncoated aluminium foil reference sample. The images in Figure 4.8 a are of the parallel of samples that was illuminated during the de-icing, and the images in Figure 4.8 b are of the parallel that was kept in the shade during de-icing.

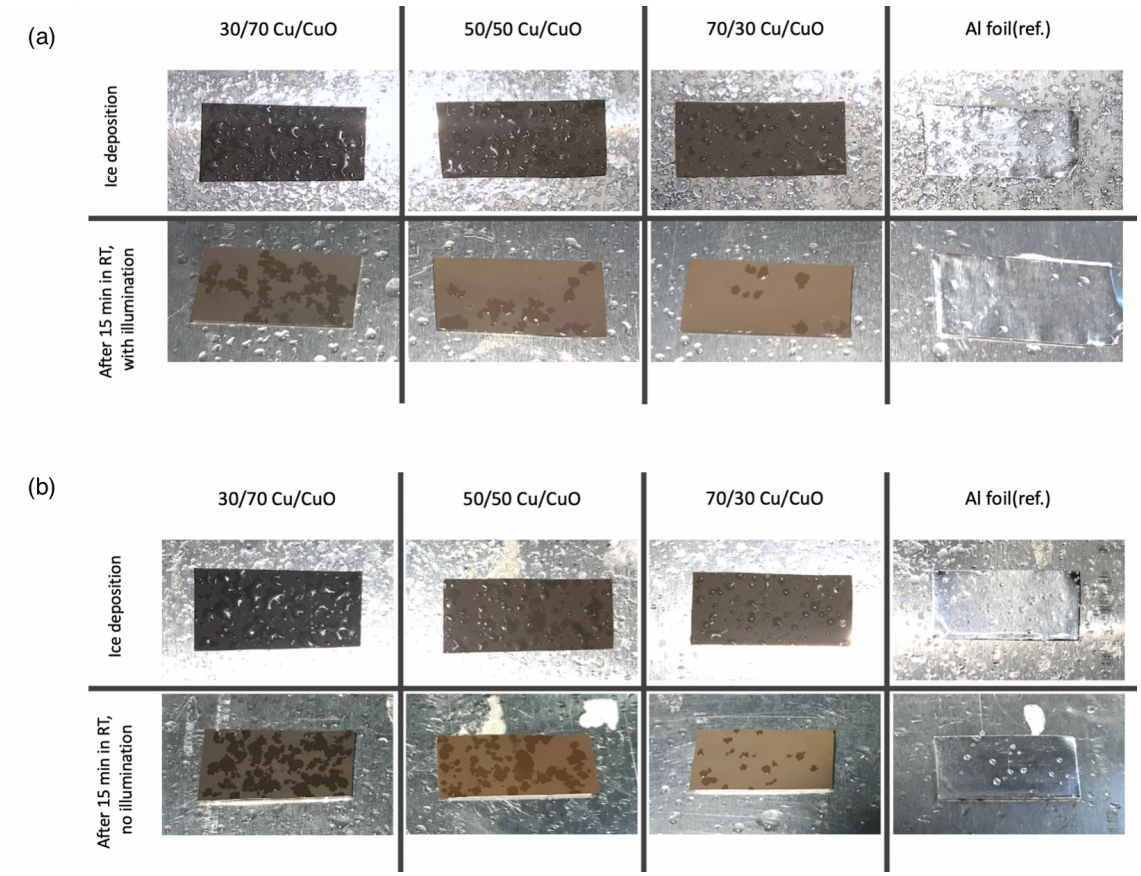

Figure 4.8: Photographs recorded of the icing and de-icing development on the three Cu/CuO prototype coating samples, and on the uncoated aluminium foil reference sample, a) with surface illumination and b) without surface illumination. For each subfigure, the top row of images shows the extent of icing on the surfaces 20 minutes after ice water deposition, before any de-icing has occurred. The bottom rows of images show the surfaces after 15 minutes of de-icing in room temperature (RT).

After approximately one minute, observations suggested that the ice had melted on all three of the illuminated Cu/CuO coating samples. At this point, there was still frozen ice on the uncoated aluminium sample, which indicates that the surface of the selective absorbers experienced more rapid rates of de-icing. As is shown in Figure 4.8, the prototype coating sample with the 70/30 Cu/CuO absorber material had the least amount of water on its surface after 15 minutes of de-icing, in both parallels. This suggests that the rate of melting, and subsequent evaporation, of ice from the surface increased with increasing metal content in the absorber. Furthermore, the illumination was shown to have a small, but positive influence on the ice melting and evaporation processes. However, in both parallels, the amount of water left on the sample surface after 15 minutes of de-icing was almost identical for the three prototype coating samples as for the uncoated aluminium foil sample. Further observations revealed that both the illuminated and unilluminated 70/30 Cu/CuO samples had completely dry surfaces after 20 minutes of de-icing. Furthermore, the evaporation

was slowest for the unilluminated 30/70 Cu/CuO sample, which was observed to be completely dry only after 30 minutes of de-icing.

4.2.2 Comparison of 50/50 Cu/CuO and SiC coatings

The following figures present the de-icing development on the surfaces of the 50/50 Cu/CuO and SiC prototype coating samples, and of the uncoated aluminium foil reference sample. The images in Figure 4.10 are of the parallel where the samples were illuminated during the de-icing, and the images in Figure 4.9 are of the parallel that was not illuminated. In both figures, the top row of images shows the extent of icing on the surfaces before any de-icing has occurred. In Figure 4.10, the images on the second and third row are taken 3 and 10 minutes into the surface de-icing process, respectively. In Figure 4.9, the images on the second and third row are taken 10 and 40 minutes into the de-icing process, respectively.

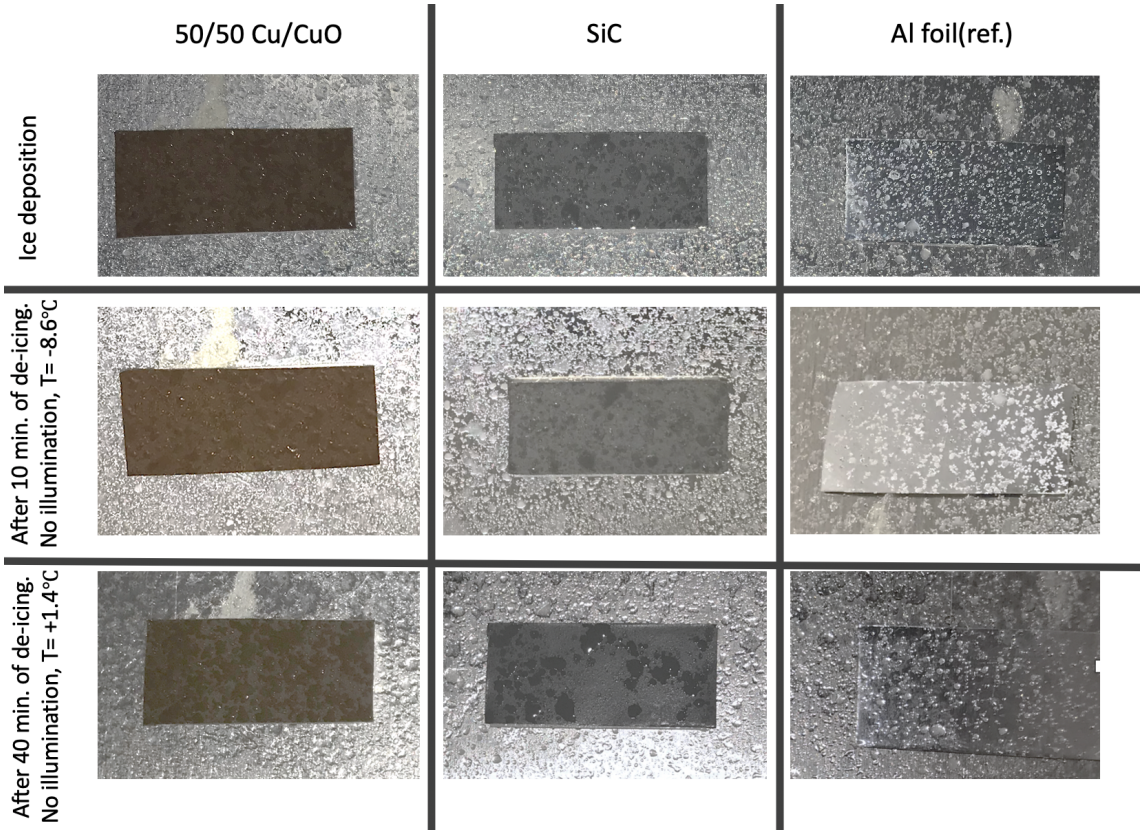

Figure 4.9: Photographs recorded of the de-icing development on the 50/50 Cu/CuO and SiC prototype coating samples, and on the uncoated aluminium foil reference sample. The top row of images shows the extent of icing on the surfaces 20 minutes after ice water deposition, before any de-icing has occurred. The second row of images shows the surfaces after 10 minutes of de-icing with surface illumination, at which point the temperature in the Styrofoam box was measured to be -8.6 °C. The third row of images shows the surfaces after 40 minutes of de-icing with surface illumination, at which point the temperature in the Styrofoam box was measured to be 1.4 °C.

As is shown in Figure 4.9, the de-icing process of the unilluminated parallel was very slow. After 10 minutes, there was still no sign of melting on any of the sample surfaces. After 40 minutes, the ice had melted on both of the coating prototype samples, while solid ice was still observed on the uncoated aluminium. An hour into the de-icing process, the experiment was terminated. At this point, the SiC prototype coating sample was observed to be completely dry, while there was moisture to be detected on both the 50/50 Cu/CuO and uncoated aluminium samples.

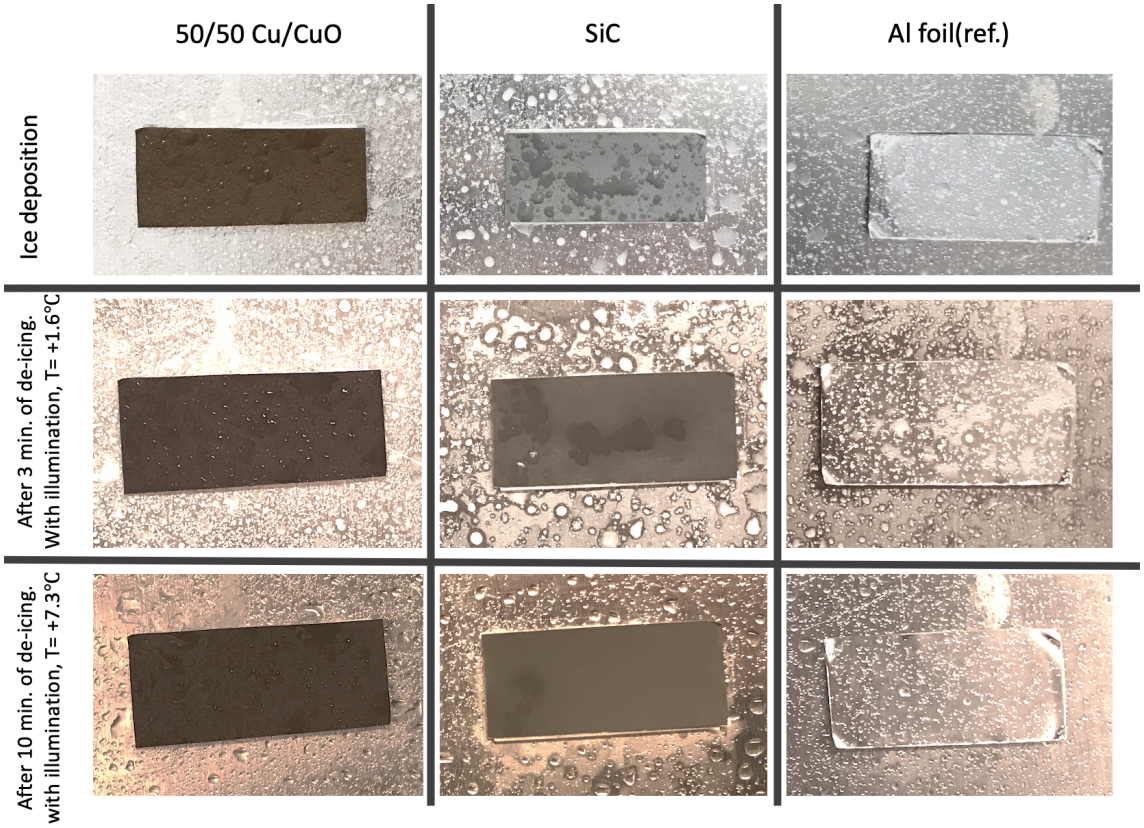

Figure 4.10: Photographs recorded of the de-icing development on the 50/50 Cu/CuO and SiC prototype coating samples, and on the uncoated aluminium foil reference sample. The top row of images shows the extent of icing on the surfaces 20 minutes after ice water deposition, before any de-icing has occurred. The second row of images shows the surfaces after 3 minutes of de-icing with surface illumination, at which point the temperature in the Styrofoam box was measured to be 1.6 °C. The third row of images shows the surfaces after 10 minutes of de-icing with surface illumination, at which point the temperature in the Styrofoam box was measured to be 7.3 °C.

The images in Figure 4.10 show that after 3 minutes of de-icing with illumination, the ice on the two coating samples had melted, and for the one with SiC as the absorber layer, some water had also evaporated. At this point, ice was still observed on the surface of the uncoated aluminium foil sample (as well as on the aluminium plate the samples are mounted to). The SiC prototype coating, uncoated aluminium, and 50/50 Cu/CuO coating samples were observed to be completely dry after 15, 25 and 30 minutes of de-icing with illumination, respectively.

4.3 Thermal characterisation

The results from the thermal characterisation of the four absorber materials are presented in Table 4.4. These include the specific heat capacities (C_p) that were measured using Differential Scanning Calorimetry (DSC) and thermal diffusivities (α) that were measured using the laser flash method, and additionally, the thermal conductivities (λ) that were calculated from these measurements. These results indicate that the SiC sample had the highest thermal conductivity of the four absorber materials. Additionally, C_p and α values were higher for the 70/30 Cu/CuO sample than the other two Cu/CuO samples, which suggests that the heat conductive abilities increased with increased metallic composition.

Some additional results from the DSC measurements, as well as details on the calculation of thermal conductivity can be found in Appendix B.

Table 4.4: Thermal properties of each of the four absorber materials. The heat capacity (C_p) and thermal diffusivity (α) values are measured using differential scanning calorimetry (DSC) and laser flash methods, respectively. The thermal conductivity (λ) values are calculated from these by the formula given in Appendix B.

Absorber material	C_p [J/gK]	α [mm^2/s]	λ [W/mK]
SiC	0.657	0.448	0.475
30/70 Cu/CuO	0.344	0.218	0.241
50/50 Cu/CuO	0.468	0.168	0.239
70/30 Cu/CuO	0.606	0.185	0.344

4.4 Optical characterisation

The optical measurements performed with the integrating sphere method produced absorbance spectra for all four of the absorber materials. These spectra can be seen in Figure 4.11, where the optical absorbance is presented as a function of the incident radiation wavelength. In general, all samples showed a high absorbance across the measured wavelengths. However, the absorbance of all three Cu/CuO samples decreased towards longer radiation wavelengths, whilst the SiC sample gave a more uniform absorbance across all wavelengths. From comparing the three Cu/CuO spectra it can also be deduced that the absorbance generally increased with increasing oxide content.

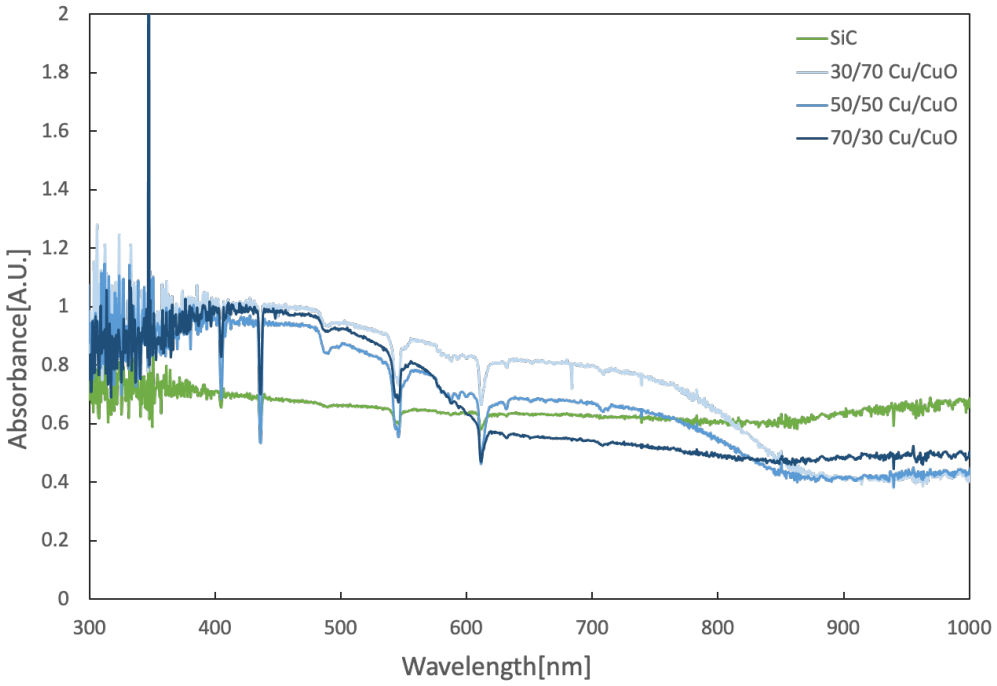

Figure 4.11: Absorbance spectra for the four absorber materials. Optical absorbance for each material is plotted as a function of the incident radiation wavelength.

By using the transmittance data from the integrating sphere measurements in a Tauc plot, the optical band gaps of the three Cu/CuO cermet materials were calculated. The optical band gaps of each of the Cu/CuO cermet materials are listed as follows:

- **30/70 Cu/CuO:** 1.65 eV
- **50/50 Cu/CuO:** 1.80 eV
- **70/30 Cu/CuO:** 1.85 eV

4.5 Powder characterisation

Figure 4.12 shows secondary electron images taken of the copper (Cu) powder particles using scanning electron microscopy (SEM) with two different levels of magnification. The images reveal that the powder consisted of mostly very small particles of approximately 1 µm to 3 µm in diameter, as well as larger agglomerates with diameters up to 300 µm. The individual particles were roughly spherical in shape, but had a somewhat uneven surface.

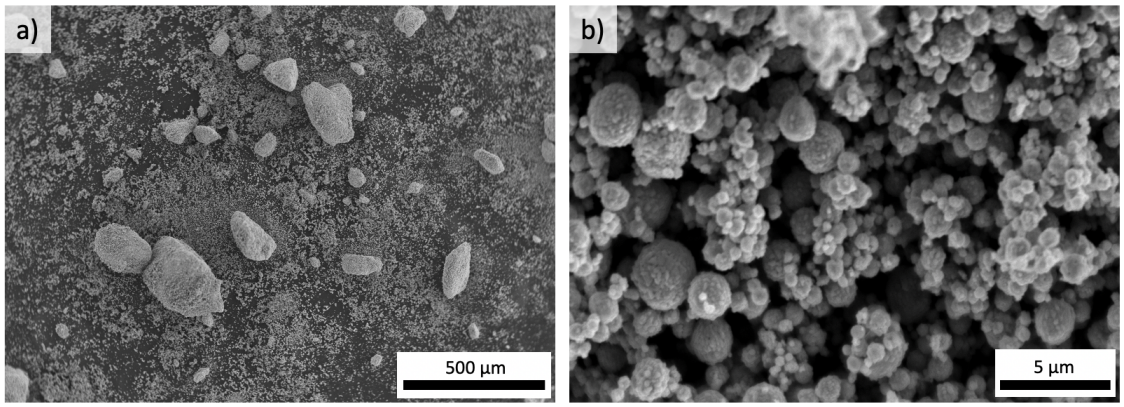

Figure 4.12: Secondary electron scanning electron microscopy images of the copper powder particles taken with a) low magnification and b) high magnification.

Figure 4.13 shows secondary electron images taken of the cupric oxide (CuO) powder particles using scanning electron microscopy (SEM) with two different levels of magnification. The lower magnification image in 4.13 a reveals a uniform distribution of particle sizes. Most of the powder particles seemed to be in the diameter range 20 µm to 50 µm, with the exception of a few larger agglomerates. The particles appeared to have very rough surfaces, with many sharp ridges.

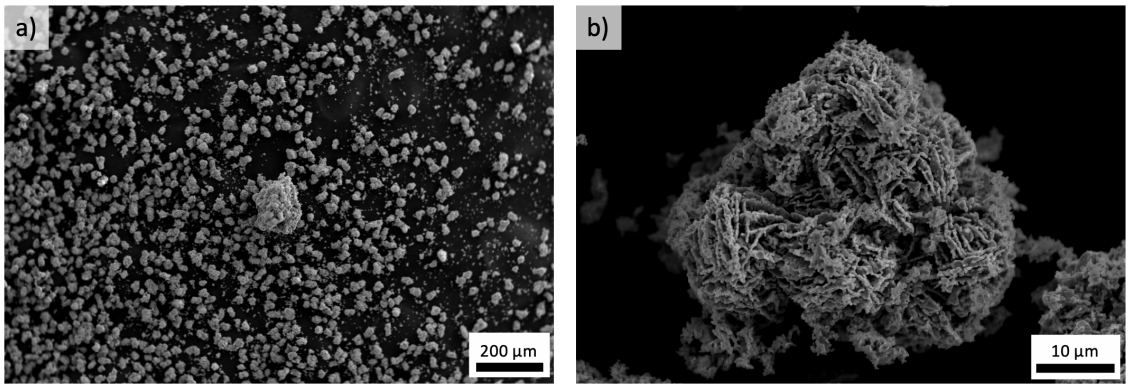

Figure 4.13: Secondary electron scanning electron microscopy images of the cupric oxide powder particles taken with a) low magnification and b) high magnification.

The particle size distributions of the Cu and CuO powders were measured by laser scattering of aqueous dispersions, and are presented in Figure 4.14. From the distribution for the Cu powder it can be deduced that more than 90 % of the metal particles were smaller than 10 µm, and that the median particle diameter was approximately 3.5 µm. The distribution also has two smaller count peaks around particle diameter 40µm and 110µm, which represent unbroken agglomerates. The median particle diameter of the CuO powder was however measured to be of a larger magnitude, at approximately 30 µm, and less than 20 % of the CuO particles were measured to be smaller than 10 µm.

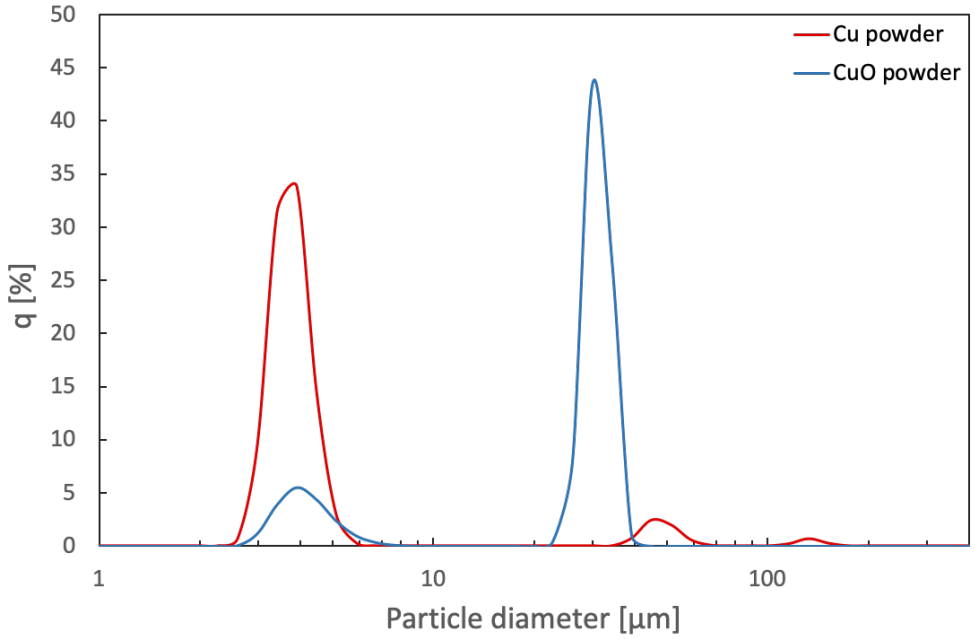

Figure 4.14: Graph illustrating the particle size distributions for both the Cu powder (red) and CuO powder (blue), with percentage particle count (q) plotted as a function of particle diameter.

4.6 Sample density

Table 4.5 gives an overview of the achieved densities of the absorber materials for each of the prepared samples. The densities of the pressed pellets were calculated from the data in Table 3.6, and these calculations can be found in Appendix C. This appendix also includes the data and formula used to calculate the densities of the absorber layers of the prototype coating samples.

The densities of the different types of samples were reasonably comparable. The SiC samples had the most variation in density between the different sample types. The calculated density of the 50/50 Cu/CuO absorber layer deviates significantly from the rest of the values, and should be considered invalid. This error is presumed to originate from the sample used to measure mass having a thinner absorber layer than the sample used to measure the absorber layer thickness.

Table 4.5: Densities achieved of the absorber materials in each type of prepared samples. *The density of the 50/50 Cu/CuO absorber layer is considered an invalid result.

Sample type	Absorber material	Density [g/cm^3]
Prototype coating	SiC	2.15
	30/70 Cu/CuO	3.27
	50/50 Cu/CuO	0.95*
	70/30 Cu/CuO	3.82
Pressed pellets, 10 mm diameter	SiC	1.87
	30/70 Cu/CuO	3.53
	50/50 Cu/CuO	3.30
	70/30 Cu/CuO	3.44
Pressed pellets, 15 mm diameter	SiC	1.61
	30/70 Cu/CuO	3.22
	50/50 Cu/CuO	3.04
	70/30 Cu/CuO	3.07

5 Discussion

This work aimed to prepare and characterise four different prototypes of a photothermal trap coating for de-icing applications. The first few sections will discuss the results in regards to the method of preparation, coating durability and obtained surface characteristics. Next, there are two separate sections where the thermal and optical characterisation results are reviewed. Finally, the de-icing characteristics of the coatings are reviewed, and put in context with other measured properties. A separate subsection is devoted to a review of the method used for de-icing characterisation.

5.1 Coating characteristics

The tape casting method was successfully used to prepare samples of prototype photothermal trap coatings. The strips of foil that were produced could easily be cut into pieces that were fit for the subsequent characterisation, without any serious breakage or detachment of the absorber layers. The thickness of the tape cast layers of the samples were reported to be in the range of 26 µm to 110 µm. Dash et al. [2] reports that the absorber layer of their prototype coating had a thickness of < 1 µm. With the increased thickness of this layer, the conduction of heat within the layer becomes more important. The reason for this is that the heat transfer to and from the thermal spreader layer is crucial to the coatings de-icing function.

From inspection of the scanning electron microscopy (SEM) images recorded of the absorber layer cross-sections (Figures 4.3 and 4.4), the inner structure of the layers could be described as rather porous. Most ceramic casting processes are followed by a sintering step that densifies the product, increasing its strength [74]. The samples prepared in this study were not heat treated in any way, and thus the final structure of the absorber layers essentially consisted of dispersed powder particles held together by a polymer network. For this reason, the tape cast layers were expected to have much lower densities than the pellet samples produced by uniaxial pressing, as pressing techniques tend to result in more densely packed bodies [74]. The results presented in Table 4.5, however, show that the tape cast and pressed samples had very comparable densities. Hence, the thermal properties measured for the pellet samples can be said to apply also for the tape cast absorber layers.

The ceramic slurries used to tape cast the absorber layers were roller mixed for approximately 16 hours. This step is crucial to any ceramic casting process, as it breaks up larger agglomerates and ensures an even dispersion of powder particles. A poorly dispersed slurry could result in tapes where the particle size increases moving down from the surface to the bottom of the tape, due to gravitational pull [75]. The

results indicate that the dispersion mixing was highly successful in the preparation of the prototype coating samples. In the characterisation of the SiC [18], Cu and CuO powders, some large agglomerates were observed. The SEM images in Figure 4.2 and Figure 4.4 show that these had been broken apart and that the distribution of particle sizes was very uniform in the prepared coatings, both across the surface and throughout the absorber layer. Additionally, the dispersion mixing promoted an even distribution of the ceramic and metal components of the Cu/CuO absorber layers, as evidenced by the energy dispersive x-ray spectroscopy (EDS) results.

5.1.1 Surface roughness

The surface profiles of the photothermal trap coatings are important to consider, as they have a significant impact on the wetting and ice adhesion properties. The profilometer results revealed both the waviness and the roughness of the coating surface (Appendix A). Waviness refers to the longer wavelength signals that describe the macrostructural peaks and valleys of the surface, while roughness refers to the shorter wavelength signals that describe the surface microstructure [76]. The former does not have any significant impact on the functionality of the de-icing coatings. Consequently, this discussion regards only the roughness of the coating samples. The SEM images in Figure 4.2 clearly show that all of the prepared coating surfaces had very rough and porous microstructures. This is reflected in the arithmetic roughness values calculated from the profilometer measurements (presented in Table 4.1). This rough surface structure can be explained with the same reasoning as the inner porosity: The lack of a densifying heat treatment left the structure of the coating with a high degree of porosity, both closed and open.

The coating sample with 50/50 Cu/CuO as absorber material was expected to have surface properties comparable to the properties of the samples with 30/70 Cu/CuO and 70/30 Cu/CuO as absorber. Still, the calculated roughness value of this sample was a lot lower than the other two. This can be explained by a difference in particle size distribution between the coatings as observed from the SEM images in Figure 4.2. These show that the average particle size of the 50/50 Cu/CuO prototype coating was a bit smaller than that of the other Cu/CuO coatings, which resulted in a less rough surface. Likely, this particle size difference stems from the 50/50 Cu/CuO ceramic slurry experiencing a greater milling effect from the dispersion mixing.

Increased surface roughness is, as discussed in Section 2.1.1, shown to increase ice adhesion, which is not favourable for a de-icing surface [28–30]. Since the de-icing function of the photothermal trap coating in part relies on the ice sliding off of the surface under its own weight, it is reasonable to believe that the coating would benefit from having a smoother surface. Following this logic, it is safe to assume that the coating with SiC as absorber material generally would experience lower ice adhesion

strength than the three Cu/CuO coatings. Additionally, the results could be used to argue that a reduction of particle size by increased dispersion mixing reduces the surface roughness of the finished coating and, in turn, weakens the ice adhesion.

5.1.2 Wetting characteristics

All of the coating surfaces were measured as having fairly high water contact angles (WCA) at every surface temperature measured, and at 5 °C, all three of the Cu/CuO surfaces fall under the definition hydrophobic (ref. 2.2). However, when the surfaces were tilted to a vertical position, the water droplets were revealed to have very strong adhesion to the surfaces. This indicates that the surfaces had a high chemical affinity to the water molecules, a property that is not compatible with the concept of hydrophobicity. One must therefore consider other explanations as to why the surfaces had such high contact angles. In Section 2.2, the strong correlations between wetting and surface roughness is reviewed in detail. From the models developed by Wenzel [39] and Cassie [40], it is implied that the wetting characteristics of a surface transform a great deal with increased roughness. Since the coating samples prepared in this study are measured to have very rough surfaces, it can be assumed that this greatly impacted their wetting properties.

The samples with 50/50 Cu/CuO as absorber material were measured to have the most stable, high WCAs across all surface temperatures. As discussed, this surface was also measured to have the least rough surface. The SiC surface, which was measured to have the second to least rough surface, also had a very high initial contact angle. From these results, it is reasonable to conclude that there was a strong correlation between surface roughness and wetting properties for the prepared coating samples. Since ice adhesion on a surface is commonly shown to decrease with increasing water contact angle [7, 14, 44], the results from these measurement could be used to argue that the 50/50 Cu/CuO surface had the most favourable wetting properties for a de-icing coating.

The contact angles of droplets deposited on the Cu/CuO surfaces are very stable in the first 30 seconds after droplet deposition. The droplets on the SiC surfaces, on the other hand, experienced a significant decrease in contact angle after deposition. In the specialisation project report [18], the author argues that this decrease in WCA on the SiC coating surface was a result of the material porosity. Namely, water from the droplet was assumed to be drawn into the coating due to capillary action in the open pores. As this phenomenon did not seem to occur on the Cu/CuO samples, the argument could be made that they had a lower degree of open porosity than the SiC samples.

The results from the measurements indicate that WCA decreased with decreasing surface temperature for all four of the samples. This is contradictory to the results achieved by the author in the specialisation project [18], where the WCA of a tape cast SiC surface was found to increase with decreasing surface temperature. There is no obvious reason for this disagreement in results. Previous research examining the temperature dependence of contact angles has concluded that there is a weak inverse correlation between the two [77, 78]. Hence, the correlation found from the measurements in this study was likely a coincidental result originating from the limited set of data.

5.1.3 Durability

As durability is one of the main challenges within the field of developing anti-icing and de-icing surfaces, the strength and hardness of the prepared coatings were also investigated. The absorber layer was occasionally observed to show some cracking during the handling of the coating samples, and parts of the layer even flaked off from the aluminium foil. This indicates that the layer was not very flexible, and that the adhesion between the two layers was undesirably weak with regards to the application purposes. The brittle nature could be explained by the low binder content of the absorber layers, at approximately 12.5 wt%. Usually, samples prepared by tape casting have a binder content of up to 50 wt% to ensure sufficient tape flexibility in the subsequent processing. Almost all of this binder content is, however, later removed by thermal decomposition step [74]. Since these samples were not heat treated in any way, the binder remained in the material, potentially obstructing the optical and thermal properties. A higher binder content could therefore have increased the coating durability, but it would also have had negative effects on the de-icing ability.

As evidenced by the results from the scratch test, the hardness of the prepared prototype coatings was very low. The porous structure of the absorber layers allowed for a substantial degree of material compression, even at low levels of applied indenter force (Figure 4.7a). Silicon carbide is considered to be a very strong material [63], and this is reflected by the high indenter force applied in order to puncture the absorber layer (Table 4.3). The coating sample with 30/70 Cu/CuO as absorber material experienced puncture at a significantly lower applied force than the other two Cu/CuO coating samples. As metallic copper is considered to be a fairly tough material [46], this decrease in hardness with decreasing metal content was expected. Still, the coating with 50/50 Cu/CuO as absorber layer was shown to be the most puncture resilient. This is thought to arise from the shift in particle size distribution compared to the other two Cu/CuO coatings that was observed with SEM imaging and discussed in Section 5.1.1. The smaller particles allowed for a denser packing, which could have improved the hardness [79].

5.2 Thermal properties

Compared to the values presented in Table 2.1, the thermal conductivities measured for the absorber materials can be described as very low. There are two factors that contribute to this. Firstly, the samples were measured to have fairly low densities, i.e. high porosity. Silicon carbide is reported to have a theoretical density of 3.22 g/cm^3 [79], which is twice as high as the density achieved in the pressed pellet samples (See Table 4.5). Since air is a very poor thermal conductor, this porosity can be assumed to have had a strong, negative impact on the thermal conductivity of the samples. Secondly, the binder used in the sample preparation is an organic polymer, a group of materials commonly categorised as thermally insulating [79]. Hence, the high binder content could be assumed to have obstructed the internal conduction of heat in the samples.

From the thermal characterisation results of the three Cu/CuO absorber materials, it was observed that both the thermal conductivity and heat capacity increased with increasing metal content in the composite. This relation is in agreement with reviewed literature [79, 80]. Moreover, the results show that the SiC absorber had both a higher thermal conductivity and heat capacity than the Cu/CuO absorbers, which is consistent with the data presented in Table 2.1.

As previously mentioned, the tape cast absorber layers of the prototype coatings were very thick compared to the coating prepared and characterised by Dash et al. [2]. Their selective absorber material is reported as having a high thermal resistance, which necessitates the inclusion of the thermally conductive layer underneath. In order to melt already deposited ice buildup, heat that is generated from photothermal conversion in surface areas with no ice has to be transported to iced areas. Since the absorber layers of the prototype coatings prepared in this study were so thick and had fairly low thermal conductivities, the argument could be made that the heat transport within this layer was too slow for the coating to function as well as intended.

5.3 Optical properties

The SiC sample was measured to have a high, even absorption of incident radiation over the entire visible light range (wavelengths 380 - 760 nm). This result corresponds well with the dark grey colour of the sample [46]. All of the Cu/CuO samples experienced an even higher absorption than SiC at shorter wavelengths. As the wavelength of radiation increased, however, the absorption dropped, especially for the 70/30 Cu/CuO absorber. In other words, the Cu/CuO material absorbed more of the high energy radiation observed as blue light, and less of the low energy radiation observed as red light. This manifested itself in the appearance of the samples as various shades of brown, darker with increasing oxide content. The high absorption values

of the Cu/CuO absorber materials could be explained by their relatively narrow band gaps of between 1.65 eV and 1.85 eV. When photons interact with such materials, more of their energy is contained in the matter than in materials with wider band gaps [45].

The optical measurements were performed on pressed pellet samples with fairly smooth surfaces. The absorption of the materials is presumed to have been even higher in the prepared coatings, due to their rough surface texture. The texture allows reflected and re-emitted radiation to bounce back and forth between the surface structures until it is eventually absorbed [45]. Section 2.3 states that a high degree of absorption in a material is a key factor for efficient photothermal conversion. The results of these optical measurements are therefore very promising with regards to the de-icing effect of the prepared coating samples.

5.4 De-icing characteristics

The results from the de-icing characterisation uncovered that the ice melted fairly quickly on all the prototype coatings when illuminated. As described in Section 1.2, the melting of a thin film of ice at the ice/absorber interface is a significant part of the de-icing function of the photothermal trap coating. From experimental observations, it was hard to tell whether the melting of deposited ice was initiated at this interface for the prepared coating, but this can not be ruled out. Additionally, the experimental procedure, as well as the transparent nature of the deposited ice, made it difficult to pinpoint the exact moment of melting. Once the ice melted, the water was observed to have a high affinity to the coating surfaces. This confirms what was predicted from the surface characterisation: The roughness of the coating prototype surfaces gives rise to strong water and ice adhesion.

The results from the icing characteristics experiment where the three different Cu/CuO prototype coatings were compared indicate that there was a minimal de-icing effect to be gained from the absorber layer of the Cu/CuO coating. The rate of de-icing and water evaporation on the surfaces was higher for the illuminated samples than the unilluminated samples. However, this effect was also observed on the uncoated aluminium sample, which indicates that there was no added effect from photothermal conversion in the absorber layer. As stated earlier, the thickness and low thermal conductivity of the this layer is thought to have been of hindrance to the heat transport within the absorber. This theory is further strengthened by the results from this de-icing characterisation. The results also revealed that the rate of de-icing increased with increasing metal content in the absorber layer. Reviewing this in the light of the optical and thermal characterisation results, this suggests that the increased de-icing effect seen in the illuminated samples was due to thermal conduction rather than optical absorption.

A separate experiment was performed to compare the de-icing characteristics of the SiC and 50/50 Cu/CuO prototype coatings. The preliminary comparison of de-icing effects on the Cu/CuO prototype coatings showed that the three of them had fairly similar de-icing abilities, and thus this comparison could be assumed to be valid for all three of the Cu/CuO coatings. The results from the characterisation indicate that both of the prototype coatings were experiencing a positive effect from the incident illumination that increased their de-icing abilities. This was evidenced by the images presented in Figure 4.10, where the ice clearly is observed to have melted on the coating surfaces at an earlier point than on the uncoated aluminium surface. Additionally, the results suggest that the de-icing and evaporation rates were higher for the coating with SiC as absorber material than the coating with 50/50 Cu/CuO. When this is reviewed in the light of the optical and thermal characterisation, it further supports the theory that the rate of de-icing increases with increased thermal conduction in the absorber.

Observations of the SiC prototype coating during the de-icing indicate that the absorber layer absorbed significant amounts of the water from the melted ice. This is evidenced by the darker areas on the coating seen in the second row image in Figure 4.10, and strengthens the theory presented in Section 5.1.2 that the surface liquid is drawn into the open porosity of the SiC absorber by capillary action. This could be of great importance with regards to the continued de-icing performance of the coating. If the surface grooves are even partially filled with water, in either solid or liquid form, this likely affects the subsequent de-icing properties of the coating.

Review of icing characterisation method

In this study, two slightly different approaches were used to characterise the de-icing properties of the prototype coatings. The approach used to compare the three Cu/CuO coating samples had a procedure identical to the one used in the specialisation project [18]. Even though the procedure did not produce results that were particularly accurate or quantifiable, they were still used to successfully compare the de-icing characteristics of the three coatings. The main disadvantage with this approach was that, since the light safe chamber was not lifted until the end of the experiment, the development of de-icing on the unilluminated coating surfaces could not be well monitored. A modified approach was later used in the comparison of the de-icing characteristics of the SiC and 50/50 Cu/CuO prototype coatings. In hopes to more clearly observe the ice melting process, the aluminium plate with attached samples was placed in a Styrofoam box together with cooling elements. The cold environment created in the Styrofoam box successfully decreased the rate of ice melting, allowing it to be more accurately monitored. Additionally, the illuminated and unilluminated parallels were characterised separately, which allowed for more accurate comparison of the separate de-icing processes. However, the heat radiation from the light bulb caused

the temperature to increase much more rapidly during the characterisation of the illuminated parallel than of the unilluminated parallel. This likely decreased the accuracy in the comparison of the two parallels. The choice of using a sample of uncoated aluminium foil as a reference surface in the characterisation was shown to be very valuable, as it gave a clearer understanding of the effects of the absorber layer.

Due to the difficulties in observing the melting of the ice, much of the results and discussion around the de-icing characteristics on the coating surfaces instead regards the surface evaporation. These are, however, separate phenomena that are not necessarily driven by the same mechanisms [81]. One should thus be careful when assuming a positive correlation between the melting and evaporation rates of water on a surface.

6 Conclusion

In this work, the technique of tape casting was successfully used to prepare prototype samples of a multilayered de-icing coating. Four different coatings were prepared, each with different selective absorber materials as the surface layer. One of the coatings was prepared with silicon carbide (SiC) as the absorber layer; the other three were prepared with copper/cupric oxide (Cu/CuO) cermet composites of varying metal content. All of the tape cast absorber layers were characterised as being fairly porous, as well as having weak adhesion to the aluminium layer underneath. As a result of these factors, the durability of the coatings were far to poor for them to be put into use as were. Further studies should thus look to other methods of preparing this type of coating that could increase the density of the absorber layer and strengthen the interlayer adhesion. Nonetheless, preparation by tape casting was demonstrated to be a simple and fair method for the purpose of a fundamental characterisation study such as this one.

The surface structure of the prepared prototype coatings were measured by stylus profilometry to be very rough. This roughness was additionally observed to decrease with a reduction of the particle sizes in the ceramic slurry, which could be achieved by prolonged dispersion mixing. The high roughness was shown to have had a strong influence on the wetting properties of the coatings, as their surfaces were measured to have high water contact angles despite being observed as having high affinity towards water. Furthermore, the open porosity of the SiC absorber layer is thought to have absorbed water from the surface by capillary rise effects. From the relations between surface roughness, water contact angle and ice adhesion, the 50/50 Cu/CuO prototype coating is shown to have the most favourable surface properties of the four candidates, with regards to the de-icing purpose.

From the thermal and optical characterisation of the four absorber materials, SiC was observed to have higher thermal conduction and lower optical absorbance than the three Cu/CuO composites. By comparing the results of the Cu/CuO characterisation, an increase in thermal conductivity, and decrease in optical absorbance, with increasing metal content was observed. All four absorber materials were measured to have low thermal conductivities when compared to literature values, and this is likely due to the strong presence of porosity and high binder content.

Two different approaches were used to characterise the de-icing properties of the prototype coatings. Neither of the approaches gave very precise results, but the experiments still provided some useful, qualitative information about the de-icing characteristics of the coating samples. All four of the coatings were observed to experience somewhat increased de-icing rates when exposed to illumination, which

indicates that they inherit the properties required for a photothermal trap coating. The coating with SiC as absorber material experienced the highest de-icing rates of the four candidates. Additionally, the rate was shown to increase with increasing metal content in the Cu/CuO composite.

7 Further work

The results from this study suggest that the coatings prepared with silicon carbide (SiC) as the absorber layer experienced more of a photothermal de-icing effect than the ones prepared with copper/cupric oxide composite as the absorber material. Further studies could thus focus on optimising the functionality of the SiC prototype coating. In order to increase the functionality and durability of the coating, alternative methods of preparation should be investigated. A suggested method for coating preparation that would give increased control of the absorber layer thickness is spray coating. Thermal preparation methods should also be looked into, as they are reported to produce high density ceramic coatings [82].

Over the recent years, several types of coatings utilising solar illumination for anti- and de-icing puposes have been developed. One example of this is a composite film prepared by Ma et al. [17], which combined the effects of photothermal conversion with superhydrophobicity. Another is the transparent nanocomposite coating proposed by Mitridis et al. [16]. The concepts presented in these articles should be reviewed if this project is to be continued.

In order to investigate the photothermal conversion of the absorber materials more precisely, alternative methods of optical and thermal characterisation should be reviewed and employed. Additionally, surface ice adhesion should be measured in order to get a deeper understanding of the correlation between this and other surface properties. Finally, the icing characterisation method needs to be further developed in order to achieve a more accurate evaluation of the de-icing ability of photothermal coatings. The deposition of larger water droplets on the samples surfaces could allow for a more precise observation of the melting process.

References

1. Parent, O. & Ilinca, A. Anti-icing and de-icing techniques for wind turbines: Critical review. en. *Cold Regions Science and Technology* **65,** 88–96 (Jan. 2011).
2. Dash, S., de Ruiter, J. & Varanasi, K. K. Photothermal trap utilizing solar illumination for ice mitigation. en. *Science Advances* **4** (Aug. 2018).
3. Brassard, J.-D., Laforte, C., Guerin, F. & Blackburn, C. en. in *Contamination Mitigating Polymeric Coatings for Extreme Environments* (eds Wohl, C. J. & Berry, D. H.) (Springer International Publishing, Cham, 2019).
4. Department of Transportation, U. S. *How Do Weather Events Impact Roads?* https://ops.fhwa.dot.gov/weather/q1_roadimpact.htm(Visited%20June%2029th%202020) (2020).
5. Gent, R. W., Dart, N. P. & Cansdale, J. T. Aircraft Icing. *Philosophical Transactions: Mathematical, Physical and Engineering Sciences* **358.** Publisher: The Royal Society, 2873–2911 (2000).
6. Lynch, F. T. & Khodadoust, A. Effects of ice accretions on aricraft aerodynamics. en. *Progress in Aerospace Sciences* **37,** 669–767 (2001).
7. *Atmospheric icing of power networks* en (ed Farzaneh, M.) (Springer, Dordrecht ; London, 2008).
8. Morgan, C., Bossanyi, E. & Seifert, M. H. Assessment of safety risks arising from wind turbine icing. en. *Boreas IV,* 113–121 (1998).
9. Cancilla, D. A., Holtkamp, A., Matassa, L. & Fang, X. Isolation and characterization of Microtox®-active components from aircraft de-icing/anti-icing fluids. en. *Environmental Toxicology and Chemistry* **16,** 430–434 (1997).
10. Jamil, M. I. *et al.* Icephobic Strategies and Materials with Superwettability: Design Principles and Mechanism. en. *Langmuir* **34,** 15425–15444 (Dec. 2018).
11. Hejazi, V., Sobolev, K. & Nosonovsky, M. From superhydrophobicity to icephobicity: forces and interaction analysis. en. *Scientific Reports* **3,** 2194 (Dec. 2013).
12. Jung, S. *et al.* Are Superhydrophobic Surfaces Best for Icephobicity? en. *Langmuir* **27,** 3059–3066 (Mar. 2011).
13. Varanasi, K. K., Deng, T., Smith, J. D., Hsu, M. & Bhate, N. Frost formation and ice adhesion on superhydrophobic surfaces. en. *Applied Physics Letters* **97** (Dec. 2010).
14. Makkonen, L. Ice Adhesion – Theory, Measurements and Countermeasures. *Journal of Adhesion Science & Technology* **26,** 413–445 (Feb. 2012).

15. Rønneberg, S., Laforte, C., Volat, C., He, J. & Zhang, Z. The effect of ice type on ice adhesion. en. *AIP Advances* **9,** 055304 (May 2019).

16. Mitridis, E. *et al.* Metasurfaces Leveraging Solar Energy for Icephobicity. en. *ACS Nano* **12,** 9 (2018).

17. Ma, L., Wang, J., Zhao, F., Wu, D. & Huang, Y. Plasmon-mediated photothermal and superhydrophobic TiN-PTFE film for anti-icing/deicing applications. en. *Composites Science and Technology* **181** (2019).

18. Lagmannsveen, A. K. *De-icing coatings based on solar illumination; preparation and characterisation* tech. rep. (Norwegian University of Science and Technology, 2019).

19. Petrenko, V. F. & Whitworth, R. W. *Physics of Ice* (Oxford University Press Inc., 2002).

20. @mtbachelor. *"A little bit of rime ice on Summit Lift towers. Crews are working their way through the prep process. #mtbachelor"* Dec. 2015. https://twitter.com/mtbachelor/status/681180235828690944 (2020).

21. Vlasveld, M. *Freezing Rain Coming to Toronto, Ottawa* en-US. 2018. https://weather.com/en-CA/canada/news/news/2018-01-20-toronto-ottawa-hamilton-freezing-rain (2020).

22. Dehghani-Sanij, A., Dehghani, S., Naterer, G. & Muzychka, Y. Sea spray icing phenomena on marine vessels and offshore structures: Review and formulation. en. *Ocean Engineering* **132.** Library Catalog: reader.elsevier.com, 25–39 (2017).

23. Gilgamesh, E. *Sublimation, Desublimation!* Feb. 2019. https://enkidugilgamesh.wordpress.com/2019/02/11/sublimation-and-desublimation-phase-changes-within-the-troposphere/ (2020).

24. Rønneberg, S. *Fundamental Mechanisms of Ice Adhesion* Doctoral Thesis (Norwegian University of Science and Technology(NTNU), 2020).

25. Matsumoto, K. & Daikoku, Y. Fundamental study on adhesion of ice to solid surface: Discussion on coupling of nano-scale field with macro-scale field. en. *International Journal of Refrigeration* **32.** Library Catalog: reader.elsevier.com, 444–453 (2009).

26. Thompson, D. *et al. Initial Development of a Model to Predict Impact Ice Adhesion Stress* in (Atlanta, Georgia, USA, 2018).

27. Fortin, G. & Perron, J. Ice Adhesion Models to Predict Shear Stress at Shedding. en. *Journal of Adhesion Science and Technology* **26,** 523–553 (2012).

28. Zou, M. *et al.* Effects of surface roughness and energy on ice adhesion strength | Elsevier Enhanced Reader. en. *Applied Surface Science* **257,** 3786–3792 (2011).

29. Kreder, M., Alvarenga, J. & Kim, P. Design of anti-icing surfaces: smooth, textured or slippery? *Nature Reviews Materials* **1** (2016).

30. Bharathidasan, T., Kumar, S., Bobji, M., Chakradhar, R. & Basu, B. Effect of wettability and surface roughness on ice-adhesion strength of hydrophilic, hydrophobic and superhydrophobic surfaces. en. *Applied Surface Science* **314.** Library Catalog: reader.elsevier.com, 241–250 (2014).

31. Rønneberg, S., He, J. & Zhang, Z. The need for standards in low ice adhesion surface research: a critical review. en. *Journal of Adhesion Science and Technology* **34,** 319–347 (Feb. 2020).

32. Work, A. & Lian, Y. A critical review of the measurement of ice adhesion to solid substrates. en. *Progress in Aerospace Sciences* **98,** 1–26 (2018).

33. Mørk, P. C. *Overflate- og kolloidkjemi - Grunnleggende prinsipper og teorier* 8. utgave (Institutt for kjemisk prosessteknologi, NTNU, 2014).

34. Marmur, A., Della Volpe, C., Siboni, S., Amirfazli, A. & Drelich, J. W. Contact angles and wettability: towards common and accurate terminology. en. *Surface Innovations* **5,** 3–8 (Mar. 2017).

35. Hiemenz, P. C. & Rajagopalan, R. *Principles of Colloid and Surface Chemistry* Third ed. (Marcel Dekker, Inc., New York, New York, 1997).

36. Marmur, A. Soft contact: measurement and interpretation of contact angles. en. *Soft Matter* **2,** 12–17 (2006).

37. De Gennes, P. G., Brochard-Wyart, F. & Quéré, D. *Capillarity and Wetting Phenomena: Drops, Bubbles, Pearls, Waves* (Springer Science+Business Media, 2004).

38. Drelich, J. W. Contact angles: From past mistakes to new developments through liquid-solid adhesion measurements | Elsevier Enhanced Reader. en. *Advances in Colloid and Interface Science* **267,** 1–14 (2019).

39. Wenzel, R. N. Resistance of solid surfaces to wetting by water. en. *Industrial & Engineering Chemistry* **28,** 988–994 (Aug. 1936).

40. Cassie, A. B. D. & Baxter, S. Wettability of porous surfaces. en. *Transactions of the Faraday Society* **40,** 546 (1944).

41. Antonini, C., Innocenti, M., Horn, T., Marengo, M. & Amirfazli, A. Understanding the effect of superhydrophobic coatings on energy reduction in anti-icing systems. en. *Cold Regions Science and Technology* **67,** 58–67 (June 2011).

42. De Gennes, P. G. Wetting: statics and dynamics. en. *Reviews of Modern Physics* **57,** 827–863 (1985).

43. Rønneberg, S., Xiao, S., He, J. & Zhang, Z. Nanoscale Correlations of Ice Adhesion Strength and Water Contact Angle. en. *Coatings* **10,** 379 (Apr. 2020).

44. Meuler, A. J. *et al.* Relationships between Water Wettability and Ice Adhesion. en. *ACS Applied Materials & Interfaces* **2,** 3100–3110 (Nov. 2010).

45. Johnsen, S. *The Optics of Life: A Biologist's Guide to Light in Nature* (Princeton University Press, 2011).

46. Callister, W. D. & Rethwisch, D. *Materials Science and Engineering: An Introduction* 8th Edition (John Wiley & Sons, Ltd, 2010).

47. Kennedy, C. *Review of Mid- to High- Temperature Solar Selective Absorber Materials* tech. rep. (National Renewable Energy Laboratory, July 2002).

48. Terazima, M. *et al.* (IUPAC Recommendations 2004). en. *Pure and Applied Chemistry,* 36 (2004).

49. Dan, A., Chattopadhyay, K., Barshilia, H. C. & Basu, B. Angular solar absorptance and thermal stability of W/WAlN/WAlON/Al2O3-based solar selective absorber coating. en. *Applied Thermal Engineering* **109.** Library Catalog: reader.elsevier.com, 997–1002 (2016).

50. Bialkowski, S. E. *Photothermal Spectroscopy Methods for Chemical Analysis* (John Wiley and Sons, 1996).

51. Jacquez, J. A. & Kuppenheim, H. F. Theory of the Integrating Sphere. en. *Journal of the Optical Society of America* **45,** 460–470 (June 1955).

52. Goebel, D. G. Generalized Integrating-Sphere Theory. en. *Applied Optics* **6,** 125 (Jan. 1967).

53. Lampert, C. M. Coatings for enhanced photothermal energy collection: Selective Absorbers. en. *Solar Energy Materials* **1,** 319–341 (1979).

54. Bogaerts, W. F. & Lampert, C. M. Materials for photothermal solar energy conversion. en. *Journal of Materials Science* **18,** 2847–2875 (Oct. 1983).

55. Musumeci, P. *et al.* Relaxation and crystallization of amorphous silicon carbide probed by optical measurements. en. *Philosophical Magazine B* **76,** 323–333 (Sept. 1997).

56. Harris, G. L. *Properties of Silicon Carbide* en (IET, 1995).

57. Liu, M., Lin, M. C. & Wang, C. Enhancements of thermal conductivities with Cu, CuO, and carbon nanotube fluids and application of MWNT/water nanofluid on a water chiller system. *Nanoscale Research letters* **6** (2011).

58. Kokoropoulos, P., Salam, E. & Daniels, F. Selective Radiation Coatings. Preparation and High Temperature Stability. en. *Solar Energy* **3.** ISSN: 10.1016/0038-092X(59)90003-9 Library Catalog: reader.elsevier.com, 19–23 (1959).

59. McDonald, G. E. Spectral Reflectance Properties of Black Chrome for use as a Solar Selective Coating. en. *Solar Energy* **17,** 119–122 (1975).

60. Márquez, A., Blanco, G., Fernandez de Rapp, M., Lamas, D. & Tarulla, R. Properties of cupric oxide coatings prepared by cathodic arc deposition. en. *Surface and Coatings Technology* **187.** Library Catalog: reader.elsevier.com, 154–160 (2004).

61. Powell, R., Tye, R. & Hickman, M. The Therma Conductivity of Nickel. en. *International Journal of Heat and Mass Transfer* **8,** 679–688 (1965).

62. Moore, J. P., Williams, R. K. & Graves, R. S. Thermal conductivity, electrical resistivity, and Seebeck coefficient of high-purity chromium from 280 to 1000 K. *Journal of Applied Physics* **48** (1977).

63. Cheung, R. *Silicon Carbide Microelectromechanical Systems for Harsh Environments* (Imperial College Press, 2006).

64. Lampert, C. M. & Washburn, J. Microstructure of a black chrome solar selective absorber. en. *Solar Energy Materials* **1,** 81–92 (1979).

65. Srinivasan, K., Shanmugam, N., Selvam, M., John, S. & Shenoi, B. Nickel-Black Solar Absorber Coatings. en. *Energy Conversion and Management* **24.** ISSN: 10.1016/0196-8904(84)90002-5 Library Catalog: reader.elsevier.com, 255–258 (1984).

66. Drozdov, A. *Aluminium: The thirteenth element* 1st edition (The RUSAL Library, 2007).

67. Flemming, C. A. & Trevors, J. T. Copper toxicity and chemistry in the environment: a review. en. *Water, Air, and Soil Pollution* **44,** 143–158 (Mar. 1989).

68. Gaetke, L. & Chow, C. Copper toxicity, oxidative stress, and antioxidant nutrients. en. *Toxicology* **189,** 147–163 (2003).

69. Aylward, G. & Findlay, T. *SI Chemical Data* 6th edition (John Wiley and Sons, 2008).

70. Raasok, E.-K. *Hydrophobic Coatings for Anti-Icing Applications* MA thesis (Norwegian University of Science and Technology(NTNU), 2014).

71. Lee, H. J. Design and development of anti-icing textile surfaces. en. *Journal of Materials Science* **47,** 5114–5120 (July 2012).

72. Cao, L., Jones, A. K., Sikka, V. K., Wu, J. & Gao, D. Anti-Icing Superhydrophobic Coatings. en. *Langmuir* **25,** 12444–12448 (Nov. 2009).

73. Alva, G., Lin, Y. & Fang, G. Thermal and electrical characterization of polymer/ceramic composites with polyvinyl butyral matrix. *Materials Chemistry and Physics* **205,** 401–415 (2018).

74. Richerson, D. W. & Lee, W. E. in *Modern Ceramic Engineering - Properties, Processing and Use in Design* 4th ed., 203–232 (CRC Press, Taylor & Francis Group, 2018).

75. Mistler, R. E. *Tape casting: theory and practice* eng (American Ceramic Society, 2000).

76. Whitehouse, D. J. *Surfaces and their Measurement* (Taylor Hobson Ltd., London, 2002).

77. Bernardin, J., Mudawar, I., Walsh, C. & Franses, E. Contact angle temperature dependence for water droplets on practical aluminium surfaces. en. *International Journal of Heat and Mass Transfer* **40,** 1017–1033 (1997).

78. De Ruijter, M., Kölsch, P., Voué, M., De Connick, J. & Rabe, J. Effect of temperature on the dynamic contact angle. en. *Colloids and Surfaces* **144,** 235–243 (1998).

79. Richerson, D. W. & Lee, W. E. in *Modern Ceramic Engineering - Properties, Processing and Use in Design* 4th ed., 447–520 (CRC Press, Taylor & Francis Group, 2018).

80. Takahashi, Y. Measurement of thermophysical properties of metals and ceramics by the laser-flash method. en. *International Journal of Thermophysics* **5,** 41–52 (Mar. 1984).

81. Gerasimov, D. N. & Yurin, E. I. *Kinetics of Evaporation* en (Springer International Publishing, Cham, 2018).

82. Herman, H. & Sampath, S. in *Metallurgical and Ceramic Protective Coatings* (ed Stern, K.) (Chapman & Hall, 1996).

83. Bird, R., Stewart, W. & Lightfoot, E. *Transport Phenomena* en (John Wiley & Sons, Ltd, 2002).

A Profilometer data and roughness calculations

The arithmetic roughness (R_a) of a surface is defined as "the arithmetic mean of the magnitude of the deviation of the profile from the mean line" [76]. The formula used to calculate this is given in Equation A.1, where y_i is the deviation from surface baseline of data point i in the surface profile data set and n is the total number of data points in the set.

$$R_a = \frac{1}{n}\sum_{i=1}^{n} |y_i| \tag{A.1}$$

The surface profiles that were measured with a stylus profilometer on prototype coating samples with SiC, 30/70 Cu/CuO, 50/50 Cu/CuO and 70/30 Cu/CuO as absorber materials are shown in Figures A.1, A.2, A.3 and A.4, respectively. Due to the long sampling length of the measurements, the profiles contain information on both the roughness and the waviness of the samples. Most of the data therefore deviate quite a lot from the initial baseline that was set (y=0 in the plots, marked by a grey, dotted line), which would result in very high roughness values if calculated over the entire profiles. For the purposes of this thesis project it was more interesting to look at the micrometer scale roughness. To achieve this, 3 mm sections were selected from parts of the profiles for each sample that experienced little to no waviness effect. The roughness of each of these isolated profile sections were calculated using Equation A.1, and are presented in Tables A.1, A.2, A.3 and A.4. The arithmetic roughness values that are reported in Section 4.1.1 are averages of the values calculated from the profile sections of each sample.

SiC

Figure A.1 presents the three surface profiles that were measured for the prototype coating sample with SiC as the absorber layer. The green boxes mark each of the profile sections used to calculate the micro-scale arithmetic roughness of the sample surface.

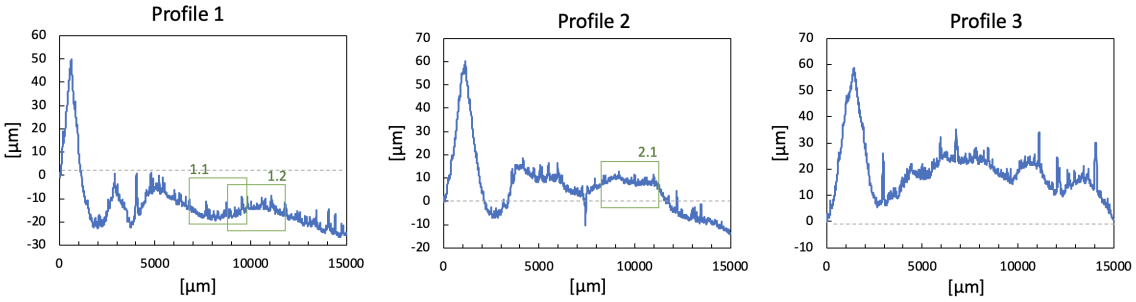

Figure A.1: The three surface profiles that were measured for the prototype coating sample with SiC as the absorber layer, where the profile sections used to calculate the micro-scale arithmetic roughness of the sample are highlighted with green boxes.

Table A.1 gives an overview of the micro-scale arithmetic surface roughness values that were calculated from each of the three profile sections of the SiC prototype coating surface profiles. The profile section identifiers in the first column correspond to the identifiers next to each of the green boxes in Figure A.1.

Table A.1: The micro-scale arithmetic roughness (R_a) values of the SiC prototype coating surface, calculated from each of the three profile sections that were isolated from the measured surface profiles of the coating sample.

Profile section	R_a [µm]
1.1	1.50
1.2	1.07
2.1	1.57
Average	1.38 ± 0.27

30/70 Cu/CuO

Figure A.2 presents the three surface profiles that were measured for the prototype coating sample with 30/70 Cu/CuO as the absorber layer. The green boxes mark each of the profile sections used to calculate the micro-scale arithmetic roughness of the sample surface.

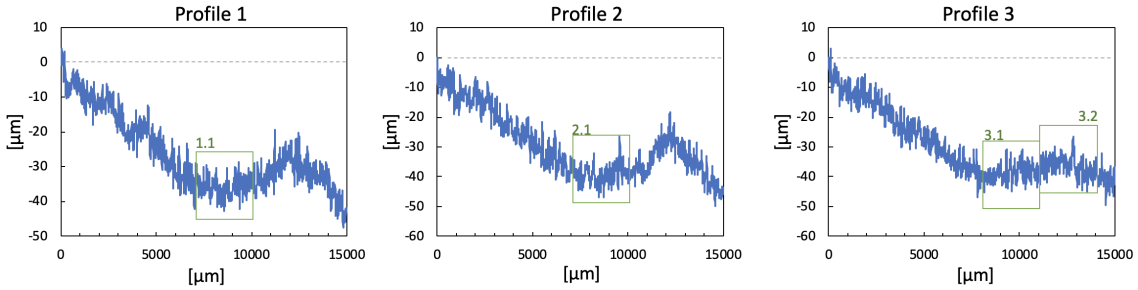

Figure A.2: The three surface profiles that were measured for the prototype coating sample with 30/70 Cu/CuO as the absorber layer, where the profile sections used to calculate the micro-scale arithmetic roughness of the sample are highlighted with green boxes.

Table A.2 gives an overview of the micro-scale arithmetic surface roughness values that were calculated from each of the three profile sections of the 30/70 Cu/CuO prototype coating surface profiles. The profile section identifiers in the first column correspond to the identifiers next to each of the green boxes in Figure A.2.

Table A.2: The micro-scale arithmetic roughness (R_a) values of the 30/70 Cu/CuO prototype coating surface, calculated from each of the four profile sections that were isolated from the measured surface profiles of the coating sample.

Profile section	R_a [µm]
1.1	2.17
2.1	2.44
3.1	2.36
3.2	2.51
Average	2.37 ± 0.15

50/50 Cu/CuO

Figure A.3 presents the three surface profiles that were measured for the prototype coating sample with 50/50 Cu/CuO as the absorber layer. The green boxes mark each of the profile sections used to calculate the micro-scale arithmetic roughness of the sample surface.

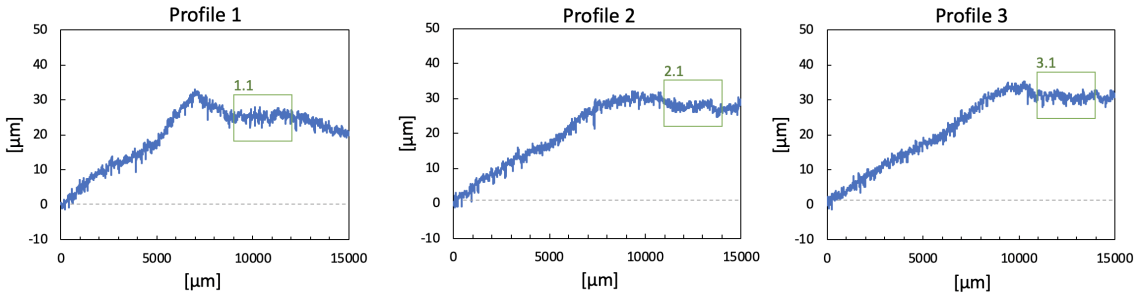

Figure A.3: The three surface profiles that were measured for the prototype coating sample with 50/50 Cu/CuO as the absorber layer, where the profile sections used to calculate the micro-scale arithmetic roughness of the sample are highlighted with green boxes.

Table A.3 gives an overview of the micro-scale arithmetic surface roughness values that were calculated from each of the three profile sections of the 50/50 Cu/CuO prototype coating surface profiles. The profile section identifiers in the first column correspond to the identifiers next to each of the green boxes in Figure A.3.

Table A.3: The micro-scale arithmetic roughness (R_a) values of the 50/50 Cu/CuO prototype coating surface, calculated from each of the three profile sections that were isolated from the measured surface profiles of the coating sample.

Profile section	R_a [µm]
1.1	0.817
2.1	0.875
3.1	0.756
Average	0.816 ± 0.059

70/30 Cu/CuO

Figure A.4 presents the three surface profiles that were measured for the prototype coating sample with 70/30 Cu/CuO as the absorber layer. The green boxes mark each of the profile sections used to calculate the micro-scale arithmetic roughness of the sample surface.

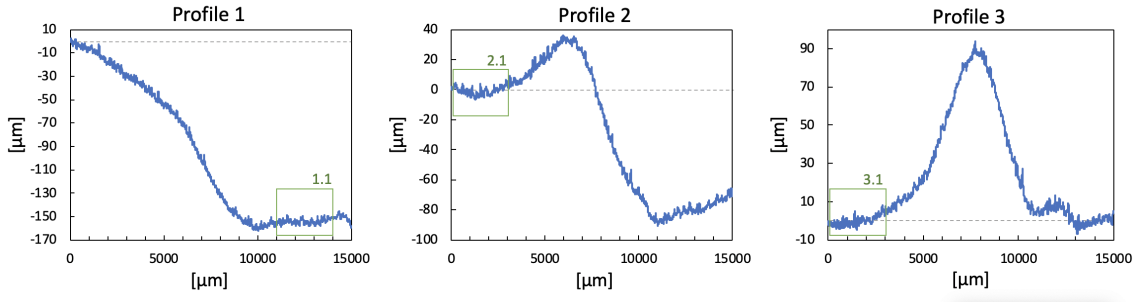

Figure A.4: The three surface profiles that were measured for the prototype coating sample with 70/30 Cu/CuO as the absorber layer, where the profile sections used to calculate the micro-scale arithmetic roughness of the sample are highlighted with green boxes.

Table A.4 gives an overview of the micro-scale arithmetic surface roughness values that were calculated from each of the three profile sections of the 70/30 Cu/CuO prototype coating surface profiles. The profile section identifiers in the first column correspond to the identifiers next to each of the green boxes in Figure A.4.

Table A.4: The micro-scale arithmetic roughness (R_a) values of the 70/30 Cu/CuO prototype coating surface, calculated from each of the three profile sections that were isolated from the measured surface profiles of the coating sample.

Profile section	R_a [µm]
1.1	1.79
2.1	2.25
3.1	2.06
Average	2.27 ± 0.23

B Thermal measurements and calculations

Differential Scanning Calorimetry measurements

Specific heat capacity (C_p) measurements were carried out by differential scanning calorimetry (DSC). Figure B.1 shows diagrams where C_p is plotted as a function of temperature for each of the four absorber materials.

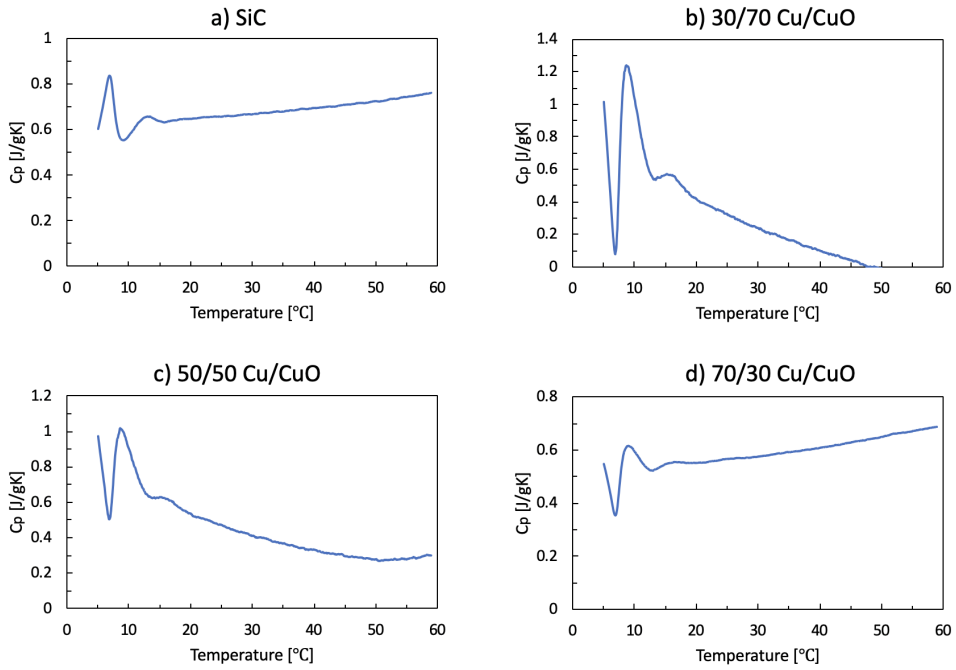

Figure B.1: Specific heat capacity (C_p) as a function of temperature for absorber materials a) SiC, b) 30/70 Cu/CuO, c) 50/50 Cu/CuO and d) 70/30 Cu/CuO, as measured from differential scanning calorimetry.

Thermal conductivity calculations

The thermal conductivity (λ) of a material at temperature T is related to the materials thermal diffusivity (α), density and specific heat capacity (C_p), through Equation B.1[83].

$$\lambda(T) = \rho(T)C_p(T)\alpha(T) \tag{B.1}$$

This equation was used when calculating the thermal conductivities of the four absorber materials from laser flash and DSC measurements, reported in Table 4.4.

C Sample density - measurements and calculations

The densities of the pressed pellet samples, as well as the density of the absorber layers of the four prototype coatings were calculated using the definition of volumetric mass densities,

$$\rho = \frac{m}{V}, \tag{C.1}$$

where (ρ) is the density, m is the mass, and V is the volume [79].

Coating prototypes

2 cm * 1 cm pieces were cut from the prototype coating samples and weighed. An equally sized, uncoated piece of the aluminium foil used in the samples preparation was also weighed, and this weight was subtracted from the weight of the coating pieces to get the weight of just the absorber layer. The thickness of the prototype coatings' absorber layers were measured while studying their cross-sections with secondary electron scanning electron microscopy (SEM). The samples weighed and the ones studied by SEM were not the exact same. Table C.1 contains the densities that were calculated, as well as the dimensions and masses that were measured and used for these calculations.

Table C.1: Measurements used to calculate the densities of the absorber layers of the four different prototype coating samples that were prepared and characterised.

Absorber material	Thickness [cm]	Surface area [cm^2]	Volume [cm^3]	Mass [g]	Density [g/cm^3]
SiC	0.0039	2.0	0.0078	0.0168	2.15
30/70 Cu/CuO	0.0026	2.0	0.0052	0.0170	3.27
50/50 Cu/CuO	0.011	2.0	0.022	0.0209	0.95
70/30 Cu/CuO	0.0046	2.0	0.0092	0.0351	3.82

Pressed pellets, diameter 10mm

Table C.2 contains the dimensions of the pressed pellet samples that were prepared in order to measure the optical absorbance of the four absorber materials, as well as their calculated densities. The heights of the samples were measured using a digital ruler.

Table C.2: Measured dimensions, and calculated densities, of the pressed pellet samples used in the optical absorbance measurements of the four absorber materials.

Absorber material	Height [cm]	Diameter [cm]	Volume [cm^3]	Mass [g]	Density [g/cm^3]
SiC	0.517	1.0	0.406	0.760	1.87
30/70 Cu/CuO	0.493	1.0	0.387	1.368	3.53
50/50 Cu/CuO	0.485	1.0	0.381	1.257	3.30
70/30 Cu/CuO	0.510	1.0	0.401	1.378	3.44

Pressed pellets, diameter 15mm

Table C.3 contains the dimensions of the pressed pellet samples that were prepared in order to measure the thermal diffusivities of the four absorber materials, as well as their calculated densities. The heights of the samples were measured using a digital ruler.

Table C.3: Measured dimensions, and calculated densities, of the pressed pellet samples used in the thermal diffusivity measurements of the four absorber materials.

Absorber material	Height [cm]	Diameter [cm]	Volume [cm^3]	Mass [g]	Density [g/cm^3]
SiC	0.375	1.5	0.663	2.435	1.61
30/70 Cu/CuO	0.419	1.5	0.740	4.343	3.22
50/50 Cu/CuO	0.404	1.5	0.714	4.255	3.04
70/30 Cu/CuO	0.486	1.5	0.859	3.575	3.07

NTNU

Norwegian University of
Science and Technology